X-Ray Dose Reduction by Application of Neural Networks for Field-Of-View Detection

Master thesis at Ulm University

Submitted by:
Maximilian Glumann
maximilian.glumann@uni-ulm.de
980505

Examiners:
Prof. Dr. Friedhelm Schwenker
Jun.-Prof. Dr.-Ing. Michael Götz

Supervisors:
Dr. Arthur Wunderlich
Heiko Hillenhagen, M.Eng.

November 26, 2025

I hereby declare that this thesis titled:

X-Ray Dose Reduction by
Application of Neural Networks
for Field-Of-View Detection

is the product of my own independent work and that I have used no other sources and materials than those specified. The passages taken from other works, either verbatim or paraphrased in the spirit of the original quote, are identified in each individual case by indicating the source.

I further declare that all my academic work has been written in line with the principles of proper academic research according to the official "Satzung der Universität Ulm zur Sicherung guter wissenschaftlicher Praxis" (University Statute for the Safeguarding of Proper Academic Practice).

I have used the following AI technologies to draft this work: "Overleaf AI Assist" using the "Writefull" model for error-checking and language quality.

Ulm, November 26, 2025 . . . .

Maximilian Glumann, student number: 980505

Acknowledgements

Abstract

Radiography is a central imaging procedure in medical diagnostics, but the ionizing x-rays involved impose an inherent risk to patients. One way to reduce this radiation is to adjust the affected area only to the region of interest, which cannot be easily determined before the measurement. Therefore, the approach of identifying the relevant field of view using a neural network on a low dose image is pursued. To evaluate the performance of the network on low dose images, a simulation of low dose computer tomography scans from normal doses is adapted in this thesis to conventional radiography. This new simulation approach results in a more physically realistic simulation than was used in previous work, which allows a more realistic performance evaluation of the networks. In addition to the evaluation of the new simulation, an exemplary U-net architecture is trained and tested on it. The results show a promising field of view detection even for simulation parameters at a quality where it is no longer manageable for humans. But for even less quality in the simulated image, even the neural network reaches its limits.

Keywords Chest Radiography, Low Dose Simulation, Field of View Detection, Neural Networks, Segmentation

Zusammenfassung

Die Röntgenbildgebung ist eine zentrale Prozedur in der medizinischen Diagnose, aber die ionisierende Röntgenstrahlung stellt dabei eine inhärente Gefahr für die Patienten dar. Eine Möglichkeit die Strahlenbelastung dabei zu reduzieren ist es, die betroffene Region auf die relevanten Teile einzugrenzen, welche allerdings vor der Aufnahme nicht so einfach eingeschätzt werden kann. Daher wird der Ansatz verfolgt die für die Aufnahme relevante Region auf einem Röntgenbild mit geringer Dosis mithilfe eines neuronalen Netzes zu bestimmen. Um die Ergebnisse des Netzes auf niedrigdosigen Bildern evaluieren zu können, wird in dieser Arbeit ein Simulationsansatz für die Computertomographie entsprechend adaptiert, um ihn auf konventionelle Röntgenaufnahmen zu übertragen. Dieser neue Simulationsansatz liefert eine physikalisch realistischere Simulation als sie in vorheriger Arbeit verwendet wurde, was eine realistischere Auswertung der neuronalen Netze erlaubt. Zusätzlich zur Evaluation der neuen Simulation, wird eine beispielhafte Architektur eines U-net darauf trainiert und getestet. Die Ergebnisse zeigen eine vielversprechende Reduktion des betroffenen Bereichs sogar für Simulationsparameter, welche für Menschen nicht mehr nützliche Bilder liefern. Bei einer noch geringeren simulierten Qualität kommt allerdings auch das neuronale Netz an seine Grenzen.

Stichwörter Thorax-Röntgenaufnahme, Simulation geringer Dosis, Sichtfeld-Erkennung, Neuronale Netze, Segmentierung

Contents

Acronyms

µAs Micro-Ampere-Seconds. 7, 12, 14, 16, 19, 23–29, 32, 33, 49, 50

CT Computer Tomography. 1, 2, 7–9, 13, 14, 47, 48

DICOM Digital Imaging and Communications in Medicine. 14, 21, 43–46, 48

FOV Field of View. 2, 3, 8, 19, 36, 40–42, 45, 46, 48, 50

JSON JavaScript Object Notation. 20, 21

PNG Portable Network Graphics. 19, 21, 29, 45, 46

1 Introduction

Since the discovery of x-rays in 1895 and the following publication of their physical properties by Wilhelm Conrad Röntgen, extensive investigations of x-ray interaction with matter have revolutionized medical diagnostics. The ability of x-rays to pass through human bodies with variable attenuation depending on the types of tissue on the path made different types of x-ray imaging possible, leading to great successes and progress in medicine. The clinical applications possible with x-ray imaging cover a wide range from non-invasive diagnosis of fractures to detecting the effects of lung diseases such as tuberculosis [13] [17] or coronavirus disease-19 (COVID-19) [5]. The technology has evolved over time, starting from conventional analog x-ray using film cassettes over digitized x-ray imaging, storage, and display using computers, all the way to the invention of Computer Tomography (CT) to reconstruct a three-dimensional image from x-ray projections in different directions.

1.1 Motivation

With an estimated total amount of 125 million x-ray applications in Germany in 2021 [1], x-ray imaging is an essential part of medical diagnostics today. Conventional thorax x-rays, for example, comprise approximately 10 percent of all x-ray applications in 2021 compared to a total of approximately 1 percent for CT scans of any body part not limited to thorax CT. Although continuous improvements and research are performed to reduce the radiation dose during CT, the increased level of anatomical information comes with a radiation exposure of a manifold of conventional x-rays. In 2021, approximately 71 percent of the overall exposure to x-rays in Germany occurred from CT applications compared to only approximately 1 percent for conventional thorax x-rays even though their relative number of applications is similar. The ongoing dose reduction in CT allows for an increase in CT applications

in favor of a decreasing number of conventional x-rays. Between 2007 and 2014, the number of conventional thorax radiographs was reduced by approximately 20 percent, while the number of thorax CT has almost doubled during the same period [10].

Nevertheless, conventional x-rays should be and therefore probably will remain the preferred option over CT whenever sufficient for diagnostic purposes because of the significantly less exposure to ionizing radiation. However, still any amount of ionizing radiation is associated with risks, as the INWORKS study [14] summarized by [8] indicates. This study gave some evidence for the linear-no-threshold-hypothesis that has already been assumed previously. This hypothesis states that the relationship between the dose of ionizing radiation and cancer mortality is linear even for low doses and does not have a threshold for which any dose below can be considered harmless.

Due to the simplicity of the process, conventional x-ray has less opportunities to be improved in order to reduce radiation exposure compared to the more complex CT. Hence, it is not surprising that more research has been published trying to reduce CT doses than there is for conventional x-rays. The difficulty is that a reduction in dose results in a reduction in image quality, as is also the case with other imaging techniques. Less radiation incident to an equal area of impact inherently leads to a loss of information compared to a higher dose, which cannot be restored otherwise because there is no other source of information in the simple setup of conventional radiography. Therefore, the most promising approach to reduce radiation exposure is to reduce the affected area.

These lower dose x-rays have a worse signal-to-noise ratio, which makes them harder to interpret by clinicians. However, artificial neural networks have proven over time to be more robust to bad imaging conditions and capable of dealing with more noisy images better than humans. This suggests applying neural networks on low dose images as far as possible to reduce the amount of radiation exposed to patients. On the other hand, normal dose radiographs are needed when they should be evaluated by clinicians. This motivates the idea of applying a neural network at low doses to detect a suitable Field of View (FOV) for normal dose imaging.

The long time goal of this work is to evaluate to what extent x-ray exposure can be reduced by a combination of a first low dose image, which is fed to a neural network

to determine the area of interest before in a second step detail is added from a higher dose x-ray with an adjusted FOV for medical diagnosis. One necessary prerequisite for this analysis is a physically plausible and realistic simulation of different x-ray dose images from a higher dose, on which this thesis focuses.

1.2 Overview

This work starts in chapter 2 with the summary of some necessary background knowledge about x-rays, the previous work [11] on which this is built up and the state of the art in the literature. Chapter 3 continues with a detailed description of the acquisition of the data used, the approaches implemented, and the design decisions in the implementation of the python toolkit used for the experiments. The results of the experiments are presented in chapter 4 and discussed in chapter 5 before chapter 6 eventually summarizes this thesis and gives an outlook to future work in a continuation of this project.

2 Background

The methods used and the experiments conducted require a basic understanding of x-rays and how they are applied in medical diagnostics. As this is not necessarily common knowledge in computer science, some basic concepts are introduced here. Furthermore, the work that has already been conducted prior to this study in [11] is presented to put this thesis into context. Finally, the state of the art in the existing literature is reviewed, which serves as the basis for the following sections.

2.1 X-ray Basics

X-ray imaging has a long history and has evolved over time since the end of the 19th century [3]. Much research has been conducted in physics to understand the properties of x-rays and in medical technology to improve the creation of x-rays as well as their application in medical diagnostics. Several introductions and summaries of x-ray imaging exist aimed at different target groups depending on the required level of detail. One such overview of x-ray imaging physics, targeted at nuclear medicine technologists, is provided as a series, where, in particular, the first part [15] covers the basic principles of x-ray production whereas the second part [16] introduces x-ray interactions and image formation. The concepts and effects to understand this thesis are summarized in the following paragraphs based on the description and explanation in [15] and [16].

X-rays for medical imaging are produced in x-ray tubes where free electrons are accelerated in a vacuum by applying a high voltage. The electrons arrive at the metal anode with high kinetic energy. When these high-energetic electrons are abruptly decelerated by interaction with atoms in the anode, the remaining energy is emitted as x-ray photons.
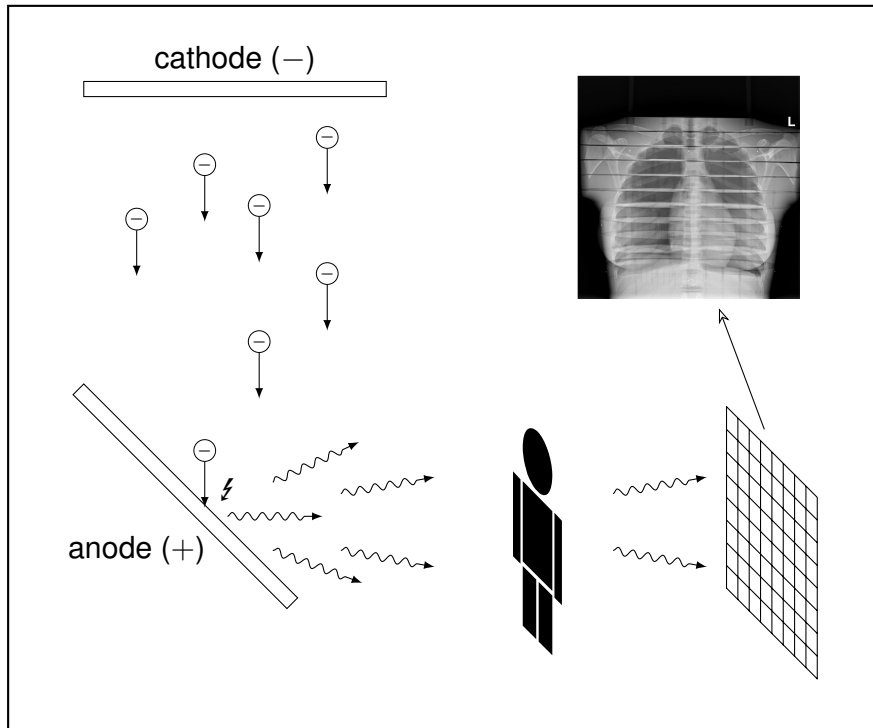
Figure 2.1: Schematic representation of x-ray generation by accelerated electrons and their interactions with the anode (visualized as lightning). The emitted photons are differently attenuated by matter such as human tissue. This difference in attenuation is recorded as a radiograph by a detector.

This photon beam is then attenuated by any matter it passes, which results in a reduction of photons. The actual attenuation depends on the type and amount of material. Finally, the attenuated beam reaches the detector, where the remaining x-ray photons are converted to another measure like visible light or electronic charge. For each element of the detector, this accumulated charge is then converted to a digital signal by an analog-digital converter, which is then captured by a computer. A schematic representation of x-ray production, its interaction with human tissue, and the resulting detection for clinical imaging is provided in Figure 2.1.

In the ideal model used here, all x-rays would be emitted from an infinitesimal small focal spot on the anode and form a uniformly spread beam in all directions. However, various physical and technical constraints restrict this in reality, resulting in various effects such as geometric blurring or the heel effect. Furthermore, the num-

ber of photons per area decreases radially from the focal spot, while the detector is flat and not curved. However, as the detector size is usually rather small compared to the distance to the focal spot, this is considered negligible here.

Given the previously described model assumptions, at each detector element the beam arrives with a specific number of photons per time unit depending on the parameters applied to the tube generating the x-rays and the attenuation on the specific path between focal spot and detector element. However, the emission of x-ray photons is still a random process and the number of photons per time is just the mean rate. As the emission of a single photon is considered independent of its direction and time, the random variable describing the actual number of photons incident to the detector element can be assumed to follow a Poisson distribution. To the image detected by the whole detector this manifests itself as Poisson noise.

Another source of noise arises from electronic noise in the digitization process, which can be assumed to be independent of the signal and is commonly modeled by a zero-mean normal distribution with a variance inherent to the device.

The x-ray photons emitted are proportional to the tube current and the time the x-ray tube is active. Hence, the exposure can be described in Micro-Ampere-Seconds (μAs). The tube voltage, on the other hand, correlates with the energy of individual x-ray photons, which in turn affects how easily they are attenuated by matter. As the latter, also known as the radiation hardness, does not directly affect the number of photons emitted, it is not varied in this work, and the device selects this parameter automatically.

For the detector, two main technologies exist on how the x-rays are detected. Either by using a scintillator, which converts x-ray photons to visible light, which is detected afterwards, or by photon counting where direct electrical effects of photons are detected. This difference is not considered relevant for this work because, regardless of the detector efficiency, only emitted x-rays can be detected.

Unlike conventional x-rays, where the detector produces a two dimensional image, a CT conceptually rotates the tube and detector around the patient and shifts along the rotation axis to retrieve three dimensional information. This stream of data over time called a sinogram is recorded, and afterwards a three dimensional image is reconstructed. This thesis only considers conventional x-ray but the simulation approach is adapted from CT where it is applied to sinogram data [2].

2.2 Previous Work

This work builds on a previous master thesis on "Optimal Field-Of-View in Low-Dose X-Ray Lung Imaging" [11], In this thesis two neural networks with a similar U-net-like architecture were implemented and compared in their ability to segment the lungs on x-rays. This segmentation was then used to estimate a minimal FOV for lung x-rays and to evaluate the respective reduction in FOV.

For training and evaluation of neural networks, a dataset of images exported from normal lung radiographs was used. As a first and simple attempt to simulate x-rays with a lower dose in the image domain, histogram matching was applied to adjust the high-dose image to be more similar to a reference low-dose measurement before noise was added. Furthermore, different types of noise and intensities were evaluated in the preceding work.

2.3 Literature Review

Although the literature on low-dose simulation for conventional x-ray images is rather sparse, there are several approaches to simulate low-dose CT images. Some of these approaches attempt to calculate the simulation directly in the image domain. As reconstructed 3D CT images can hardly be compared with conventional 2D x-ray images, this approach appears unsuitable for the use case of this thesis. However, other papers describe the simulation of low-dose CT images using a transformation of the raw sinogram data of CT scanners. This sinogram data records the measurements of the x-ray detector during the rotation over time, which is physically similar to the data returned from conventional x-ray. While the sinogram describes measurements of x-rays over a temporal dimension, in conventional x-ray a second spatial dimension is represented.

This similarity between sinogram data and conventional x-ray images allows the adaption of simulation approaches for low-dose CT images which rely on sinogram data instead of reconstructed CT images.

One such simulation approach uses a binomial distribution to simulate the thinning of photons from a higher dose measurement [2]. This binomial thinning is applied

to sinogram data, and if the sinogram is not directly accessible from a device, a reconstructed image is transformed back into a sinogram. After the application of low-dose simulation to the sinogram, this modified data is then reconstructed again to gain a simulation of a low-dose CT image.

3 Methods and Experiments
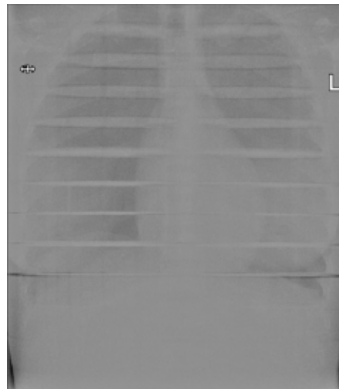
This chapter outlines the applied methods and conducted experiments, together with an overview of the data used throughout this thesis. In particular, some of the most important implementation aspects and design decisions of the python package provided with this thesis are summarized at the end of this chapter.

3.1 Data
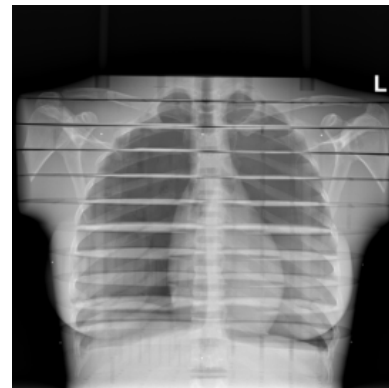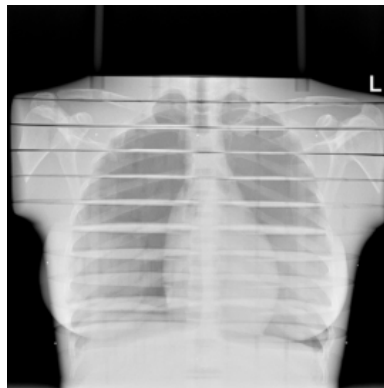
To simulate low-dose X-ray imaging in section 3.2, phantom thorax radiographs were acquired at Ulm University Hospital. A subset of these images had been previously recorded during previous work [11]. For this previous study, the images were cropped to focus on the lung region while minimizing surrounding anatomy. Exposures were performed at varying radiation doses to allow for comparative analysis. This dataset is referred to as "PhantomNoAir" in the following.

In addition to previously available phantom data, additional x-rays of the phantom thorax were made during this work to be more similar to the images in the training dataset, where most of the images cover not only the lungs but also the surrounding area and even some air. Similarly, different doses of x-rays were applied during the creation of additional phantom images to be used to evaluate low-dose simulation. In the following, this dataset is referred to as "PhantomAir".
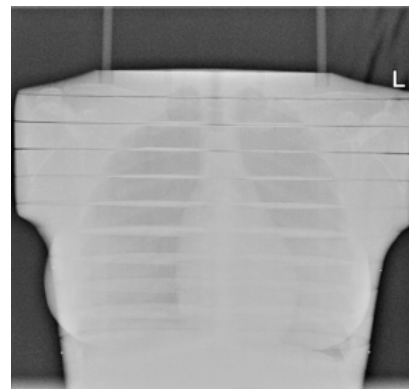
Every radiograph created during this work was made with a "Multix Fusion Max" manufactured by "Siemens Healthineers" containing a "Pixium 4242 RC-e" detector manufactured by "Trixell" [18]. This detector uses a Cesium Iodide Scintillator to translate x-ray photons to visible light, which is then detected by photo-sensitive detectors at a maximum resolution of $2860{\times}2874$ at $17{\times}17$ inches.

(a) PhantomNoAir radiographs previously produced for [11] at exposures between 650 µAs (left) and 4120 µAs (right)

(b) PhantomAir radiographs between 640 µAs (left) and 2400 µAs (right).

(c) "no x-ray" approach by shielding all x-ray with one (right) or two (left) lead aprons.

Figure 3.1: Different examples of phantom radiographs at the lowest and highest exposure respectively.

As already described previously in section 2.3, the low-dose simulation approach for CT by Elhamiasl et al. [2] was adapted for conventional x-ray in this work. The simulation algorithm described in the paper is calibrated with air scans at different doses. Therefore, more data was collected at Ulm University Hospital without any other attenuation other than air, again at different doses. This dataset is referred to as "AirOnly" in this thesis.

Although the simulation algorithm describes ways to estimate the noise parameters for electronic noise from air only recordings, additional "no x-ray" recordings were imitated. These are created by placing one and two lead aprons, which are typically used to protect humans from radiation, between the x-ray tube and the detector. The resulting image is shown in Figure 3.1. This is intended to estimate the electronic noise, while the x-ray signal and accordingly quantum noise are reduced as much as possible in the given device setup. These no x-ray recordings exist with and without the phantom as additional attenuation to estimate how much x-ray is incident even after the lead shielding.

For the implementation and training of neural networks, as described in section 3.4.1, the same data as described in [11] from [6] [17] [9]. The data is preprocessed as described in [11].

3.2 New Simulation Approach: Photon Thinning

One major contribution of this thesis is the introduction of a new approach for low dose x-ray simulation inspired by [2] as an additional approach to histogram matching as described in [11].

The low dose simulation algorithm for CT scans as described in [2] consists generally of three steps and an initial calibration step to fit the parameters used in the following steps to the device in use.

In a first step, every data sample from the scan is converted into the equivalent number of x-ray photons incident to the corresponding detector element. During the second step, the number of photons is "thinned" according to a binomial distribution, and noise is added as compensation for noise reduction during thinning. The last

step is the reconstruction of image data from thinned photon data, which is the inverse process to the first step.

In contrast to [2] where only a single CT device is considered, steps one and three are adapted for conventional x-ray instead, due to differences in the representation of the data. Adjustments and additional calibrations are necessary to support different devices. Among other options, it is necessary to consider the reference between values and intensities, in particular if data values are represented linearly or log-converted. Another important consideration is any form of post processing performed by the device during or its internal processing or by accompanied software.

For the scope of this thesis, this conversion has been reverse engineered for the device used for the phantom data described in section 3.1. The availability of these data as Digital Imaging and Communications in Medicine (DICOM) files, which contain image data as well as x-ray metadata, was the basis of the conversion process described in the following.

The conversion is applied in two parts with an equivalent exposure in µAs as an intermediate representation. The conversion of raw DICOM data to exposure is achieved by an empirically discovered exponential relation from phantom data at different exposures, as shown in Figure 3.2. The parameters a, b of this exponential $y = a \cdot \exp(b \cdot x)$ are determined from two samples $(x_1, y_1), (x_2, y_2)$, where x is the exposure and y is the corresponding value. The conversion of raw data to exposure is then described by the inverse

$$y = a \cdot \exp(b \cdot x) \Leftrightarrow x = \frac{\ln\left(\frac{y}{a}\right)}{b} \tag{3.1}$$

applied to every single pixel. The purpose of this conversion is on the one hand to invert the data and on the other hand to create a linear relation between intermediate values and exposure, which directly relates to the x-ray dose.

As a preparation for the next conversion from exposure to number of photons, figure 3.3 shows the relation between mean and variance of noise in homogeneous noise patches, only attenuated by air when possible. As motivated previously in section 2.1, the noise model is the sum of quantum noise following a Poisson distribution and electronic noise following a zero-mean normal distribution [2]. Consid-
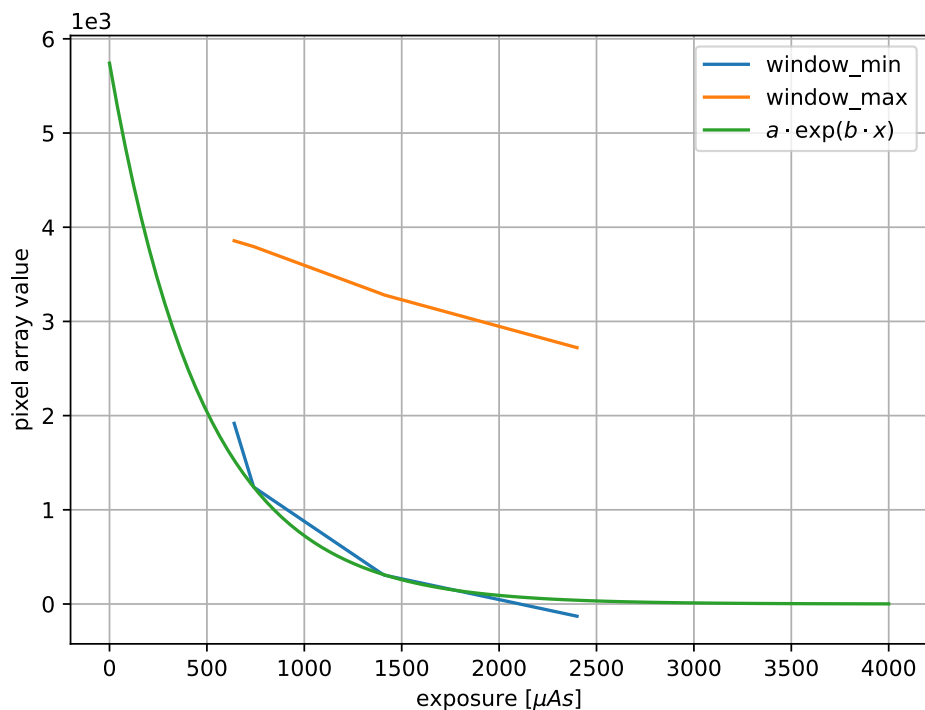
Figure 3.2: The relation between exposure in and the value range in phantom radio-
graphs. The minimum value and the maximum value of the window of
pixel values. The approximation of the minimum value by an exponential
function used for conversion is shown as well.
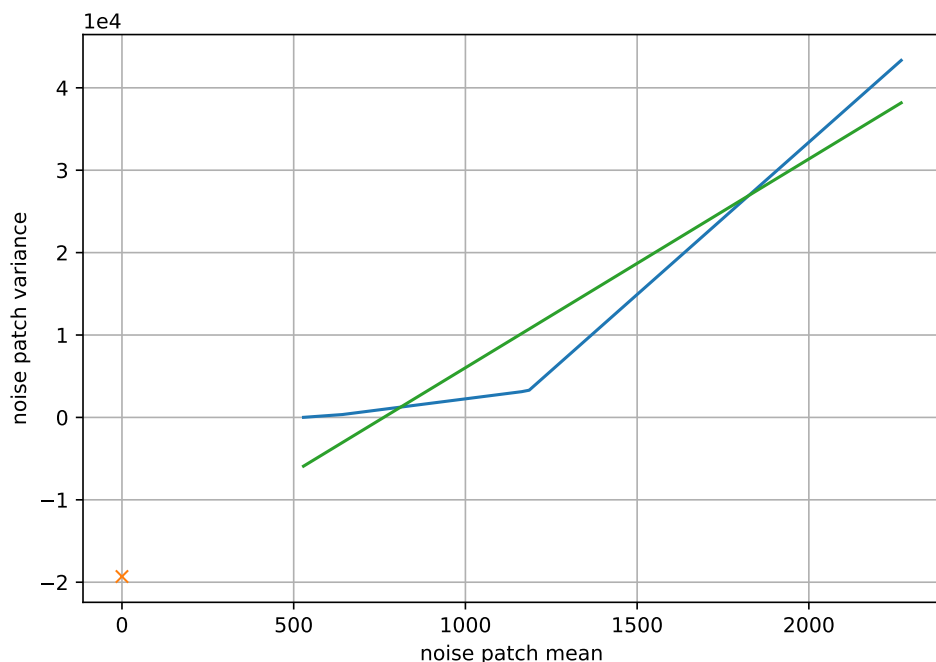
Figure 3.3: The relation between mean and variance in noise patches of phantom radiographs converted to the corresponding exposure in μAs. The data points are plotted together with a least squares approximation and a linear extrapolation at zero mean.

ering that both distributions are stochastically independent, the total variance is the sum of both individual variances. Electronic noise is assumed constant and independent of the signal and, for quantum noise, Poisson assumes a variance equal to the mean equal to its parameter λ that describes the medium rate of photons incident to a single pixel during the time of measurement. These assumptions give an expected relation between the mean μ and the variance σ^2 of $\sigma^2 = m \cdot \mu + \sigma_e^2$, where σ_e^2 denotes the variance of electronic noise. A value of $m = 1$ indicates an image represented in the number of photons, because then the variance and mean of the Poisson noise are equal to λ.

In figure 3.3 the approximation of $\sigma^2 = m \cdot \mu + \sigma_e^2$ using least squares shows indeed a mostly linear relation, but it is offset so that the estimated σ_e^2 would be negative, which is impossible. The most likely explanation for this is a noise reduction procedure that is already performed by post-processing in the software of the x-ray device. The device and its software are an unknown black-box, so it is difficult to identify reliable information about the post-processing. In the following part of this section, the noise reduction of the device is considered to reduce the variance by a constant. To continue with the conversion on approximately raw data, a zero mean normal distribution is added to the exposure representation with a variance of $|\sigma_e^2|$ estimated by least squares. After this compensating offset, $\sigma^2 = m \cdot \mu$ is assumed.

All of the x-rays mentioned in section 3.1 were made with the same device and show the same behavior that results in an approximation of negative electronic noise. The correction by adding noise compensates for this as much as is possible without knowing more internal manufacturer details about the post-processing of the device. One disadvantage of this assumption is that σ_e^2 is supposed to be 0 during photon thinning. An alternative approach to determine electronic noise is to analyze "no x-ray" scans. However, this electronic noise estimation would need to be added to the exposure intermediate as well, as it appears to be non-existent, or at least not discoverable after post-processing.

The division of intermediate exposure values for every pixel, by the slope m of the variance relative to the mean, results in a new variance $\sigma_{new}^2 = \frac{\sigma^2}{m^2}$ and a new mean $\mu_{new} = \frac{\mu}{m}$ for each radiography at a given exposure. This adjusts the slope between the new mean and variance to be approximately one, as expected for the number of photons. The resulting relation is visualized in Figure 3.4
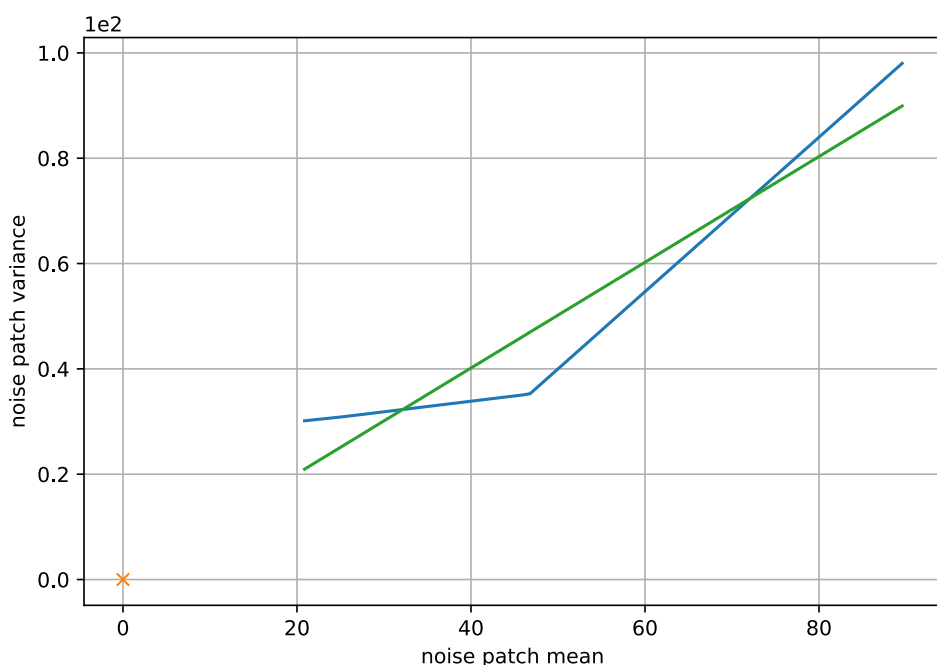
Figure 3.4: The relation between mean and variance in noise patches of phantom radiographs converted to the number of photons. The data points are plotted together with a least squares approximation and a linear extrapolation at zero mean.

Given the number of photons, the photon thinning formula from equation 11 in [2] can be applied almost identically

$$I_{sim} = B\left(I_{photon}, \frac{\alpha}{\beta}\right) + P\left(\left(1 - \frac{\alpha}{\beta}\right) \cdot \sigma_e^2\right) - \sigma_e^2 \tag{3.2}$$

where α is the simulated exposure, β the original exposure and B and P are binomial and Poisson distributions, respectively.

The adaptation of this thinning approach to pure image data such as grayscale images loaded from Portable Network Graphics (PNG) files requires some assumption about the parameters that cannot be calibrated from the dataset images. In case of the experiments in this thesis, the following properties and parameters are assumed.

First, the relation between x-ray intensity and pixel value is assumed to be linear, the maximum pixel value is equal to no x-ray, and the minimum value is equal to the exposure at an exposure of 4000 µAs for every image. In this way, the exposure representation of the image can be calculated by inverting and scaling.

Second, the photon representation is assumed to be equal to the exposure representation. The exposure representation cannot be scaled to fit photons because of unknown parameters. Therefore, the results of these experiments will be quantitatively different from the reality, but a qualitative similarity is assumed.

3.3 Field of View Reduction

The thinning approach as explained in section 3.2 was applied to the segmentation dataset mentioned in section 3.1 with different parameters. The transformed dataset was then used to train the MONAI U-net model implemented and presented in previous work [11]. For the evaluation of the neural network, the same metrics as in [11] have been applied. Especially overreach as unnecessary but covered areas and underreach as necessary but uncovered areas are analyzed together with the FOV reduction that would have been achieved by the network on the test images. Training of every network with different parameter configurations was performed for 50 epochs.

3.4 Implementation of Python Toolkit

Another contribution of this thesis is the improvement and extension of the code from previous work [11]. The focus was to create a Python (version 3.14) package `xray_fov` with structured code that is easily reusable and extendable during this and future work. The two major design decisions and the concepts implemented are explained in this section. This Python package and the Jupyter notebooks (version 7.5.0) [7] used throughout this thesis are available on GitHub [4]. The exact dependencies used are fully documented in the python package.

3.4.1 Management of Trained Weights

The code of the previous work [12] already implemented different network architectures, data loaders applying different transformations, and hyperparameter configurations. Due to the high number of possible combinations, a more structured approach is implemented during this work to keep the trained weights and related meta information organized. Another advantage of the new refactored implementation is the reduction in code duplication compared to [12].

The `nn` module of `xray_fov` comprises the network architectures, optimizers, parameter configurations, as well as a dataset and data loader that can be used with different transformations, especially to simulate low dose images in multiple ways. The parts are network architectures, optimizers, data transformations, and data sources. A name is assigned to each variant of each part, allowing the total configuration to be specified by the names of its parts together with their parametrization.

When the desired model is created and trained given the utility function in the `nn` module, a hash of the entire configuration is calculated which serves as a unique identifier. Currently a "SHAKE128" hash of length 8 is used from the `dict_hash` (version 1.3.7) python package to deterministically determine the hash of the parameter dictionary, but any other hash algorithm could be used as long as the probability of name conflicts is low enough relative to the number of desired configurations. In files with names that contain this hash, the configuration and all relevant parameters are stored in the corresponding JavaScript Object Notation (JSON) files, while the trained weights and the optimizer are stored in PyTorch (version 2.9.1)

specific binary files. This hash identifier is used to load the model, optimizer, and data specification, as well as the trained parameters, solely by file lookup. The advantage of this approach is that a single hash identifies every part of configuration, preventing mismatches, for example, between architecture and trained weights. At the same time, its usage remains flexible and extendable without code duplication. Furthermore, the human-readability of JSON files allows one to inspect all parameters related to a hash at any time.

3.4.2 Separation of Data and Operations

This concept is implemented in the `data` module of `xray_fov`. The core of this is the class `OperableData` that encapsulates a dictionary initially fed with some basic data. Any other data must be computable from these basic data. `OperableData` automatically calls operations to derive further data when requested, and the operations are maintained separately from the data. Operations are standardized member functions collected in classes that allow Operations to be overwritten, combined, and extended flexibly.

Whenever an index or member of `OperableData` is accessed, the basic data dictionary is searched to determine whether the data is already available and returned in this case. Otherwise, the function with the corresponding name in the provided operations class is called, and the result is returned. If caching is enabled, the basic data dictionary is extended by the calculated result. For every call to an operation, the parameter list is automatically extended by adding `OperableData` itself, so that the operation can rely on other existing data and operations and benefit from caching. In case of a member call to `OperableData` with non-empty arguments, caching is automatically disabled for now to limit the complexity, but the concept could be extended to support caching with parameters as well, if this might become necessary.

An essential advantage of this separation of data and operations allows switching between different operations depending on the basic data while the data access usage interface is transparently abstracted by `OperableData`. For example, the `data` module implements different operations depending on whether DICOM files or grayscale images loaded from PNG files are used as underlying data.

4 Results
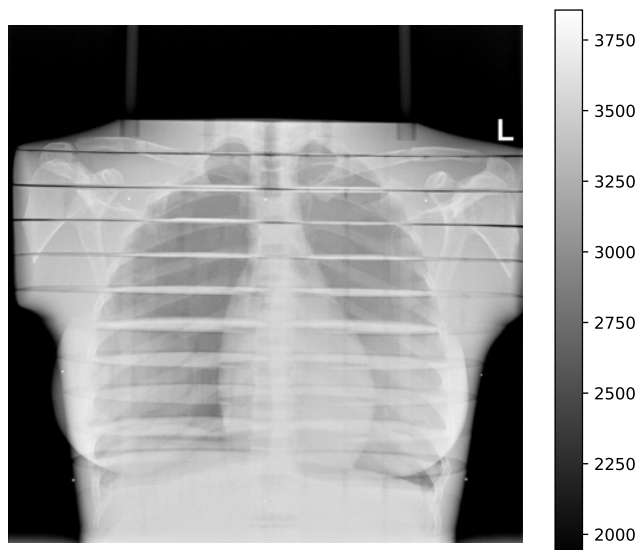
The results of the experiments and their evaluation are presented in this chapter. In particular, the new simulation approach is evaluated and compared to the previous baseline approach by histogram matching from [11].

4.1 New Simulation

The conversion steps and photon thinning as explained in section 3.2 were applied to both phantom datasets PhantomAir and PhantomNoAir, respectively, as well as to the AirOnly dataset described in section 3.1.

All intermediate representations during the conversion of a phantom x-ray at 640 µAs are depicted as an example in Figure 4.1. Compared to the raw image, the exposure representation is optically inverted, as expected. For historical reasons from the times of radiograph recordings on film, they are still commonly represented as in the raw image. Therefore, the exposure representation might seem unfamiliar at first, but it allows for easier and more intuitive computations. Unsurprisingly, the photon representation looks similar to the exposure representation, as it is only scaled with added noise, but of course, they differ in their value range and noise parameters.

The qualitative results of photon thinning applied to all PhantomAir radiographs are displayed in Figure 4.3 compared to their photon representation in Figure 4.2. Every x-ray is depicted as a pair of photon representations before and after thinning together with a homogeneous noise patch. The thinning of photons is parameterized to simulate different exposures to a constant exposure of 600 µAs. Visually, the simulated images are very similar to each other, and the mean and variance of

(a) Raw pixel data.
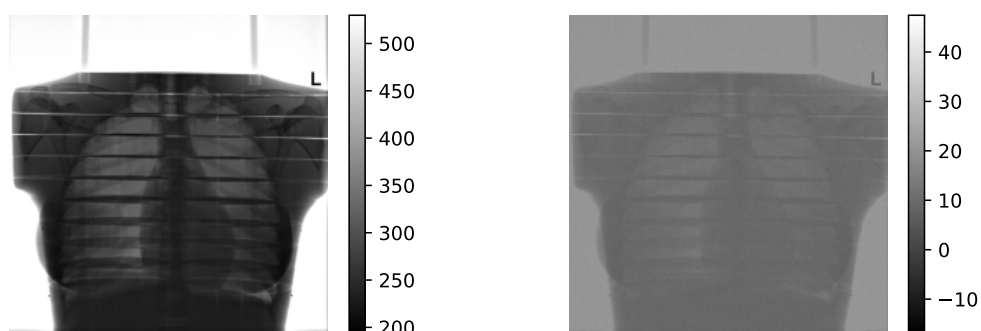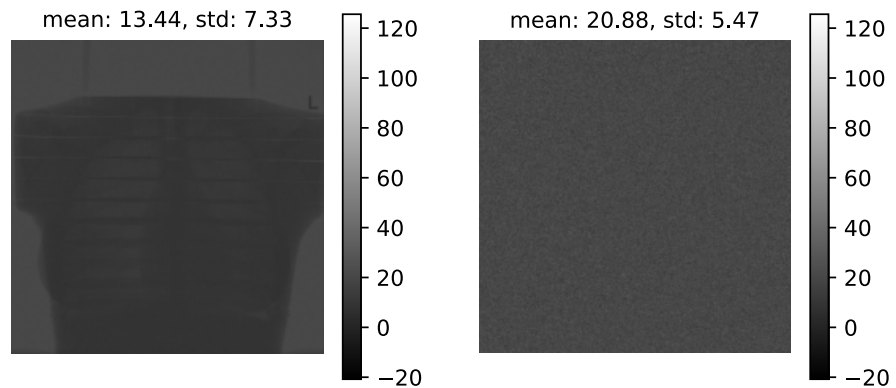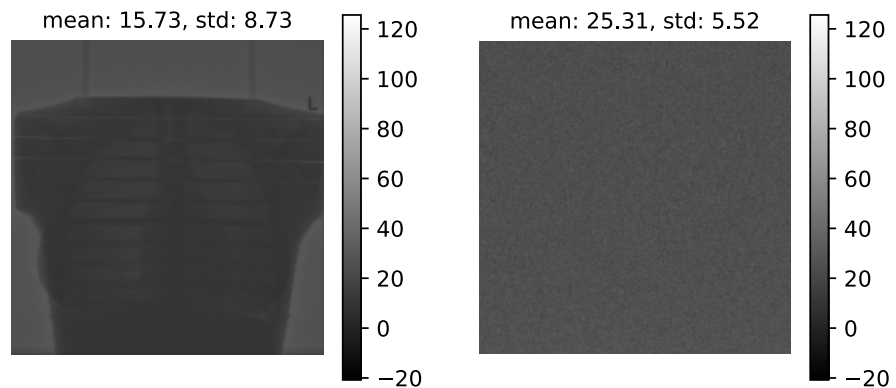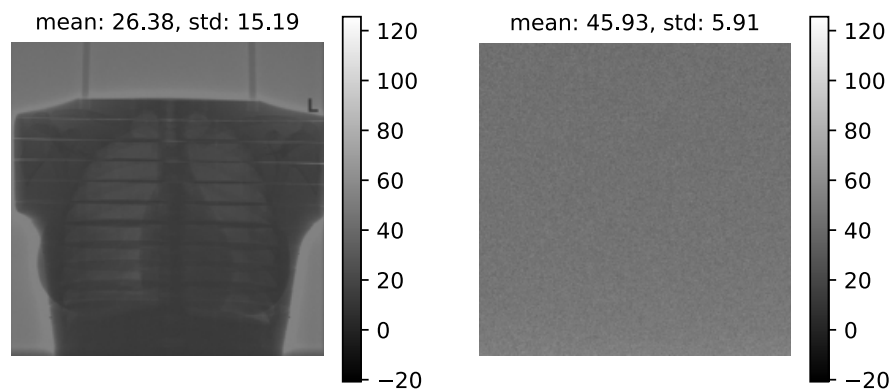
(b) exposure representation in μAs.   (c) Representation as number of photons.

Figure 4.1: All intermediate representations of a radiograph from raw pixel data to photon representation via an intermediate exposure representation. This is shown for an example phantom radiograph at 640 μAs.

(a) Photons at 640 µAs.


(b) Photons at 740 µAs.

(c) Photons at 1390 µAs.
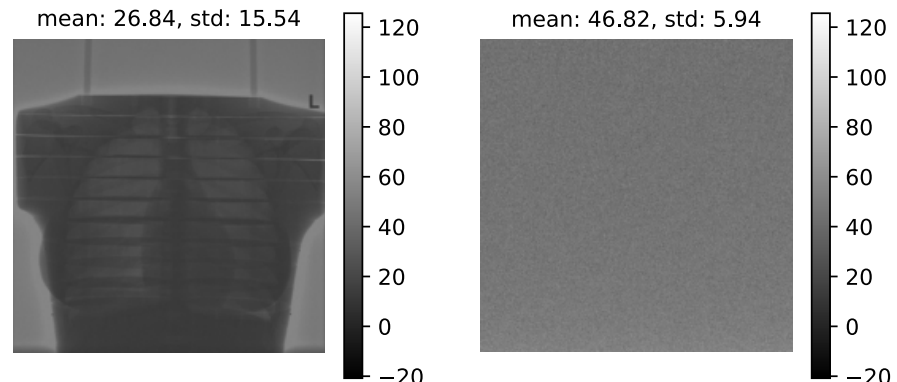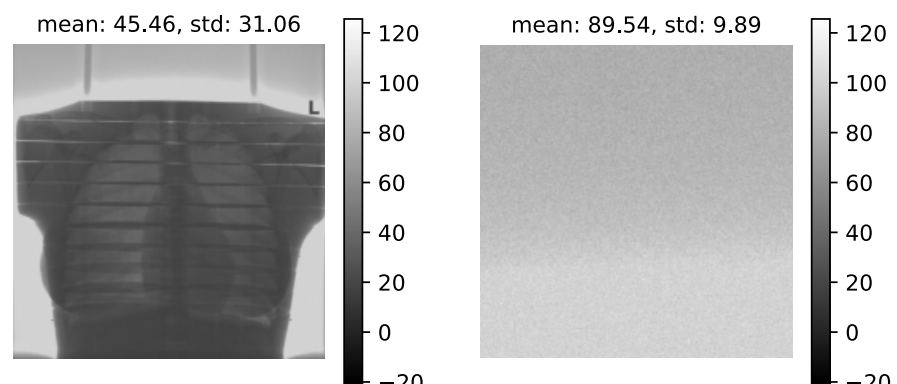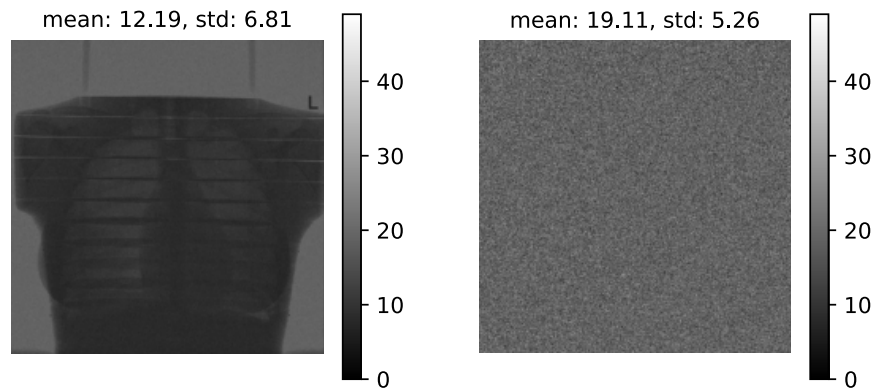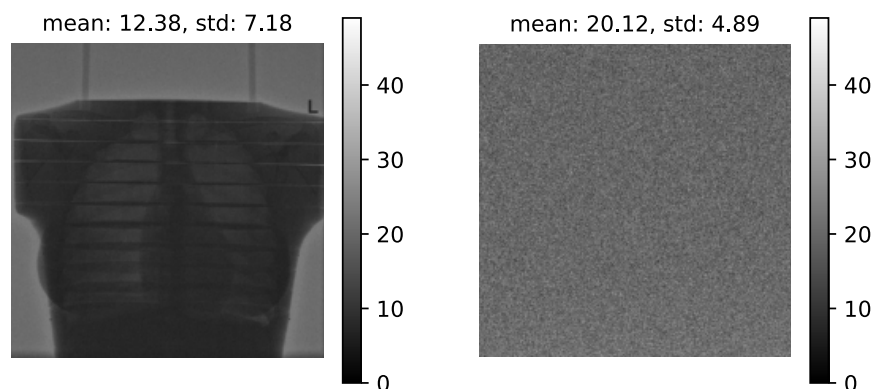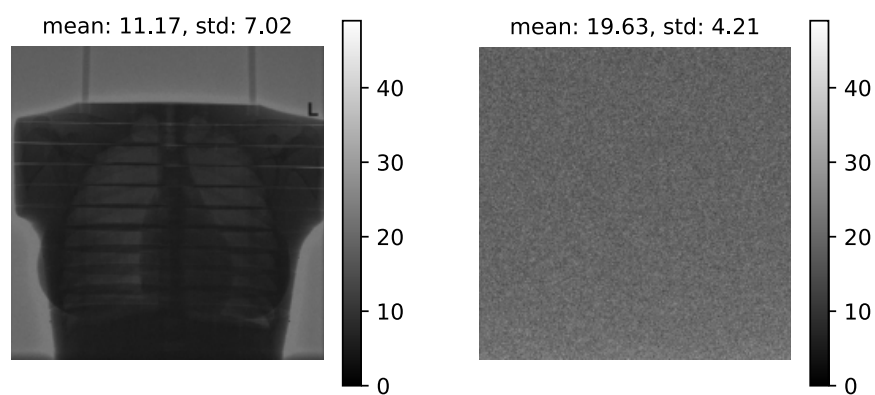
(d) Photons at 1410 μAs.

(e) Photons at 2400 μAs.

Figure 4.2: Phantoms at different exposures ranging from 640 μAs to 2400 μAs after conversion to the representation in number of photons. Every image is shown pairwise with a noise patch cut out at the top of the image between the two sticks holding the phantom in place.

(a) Thinned from 640 μAs.

(b) Thinned from 740 μAs.

(c) Thinned from 1390 μAs.

(d) Thinned from 1410 µAs.

(e) Thinned from 2400 µAs.
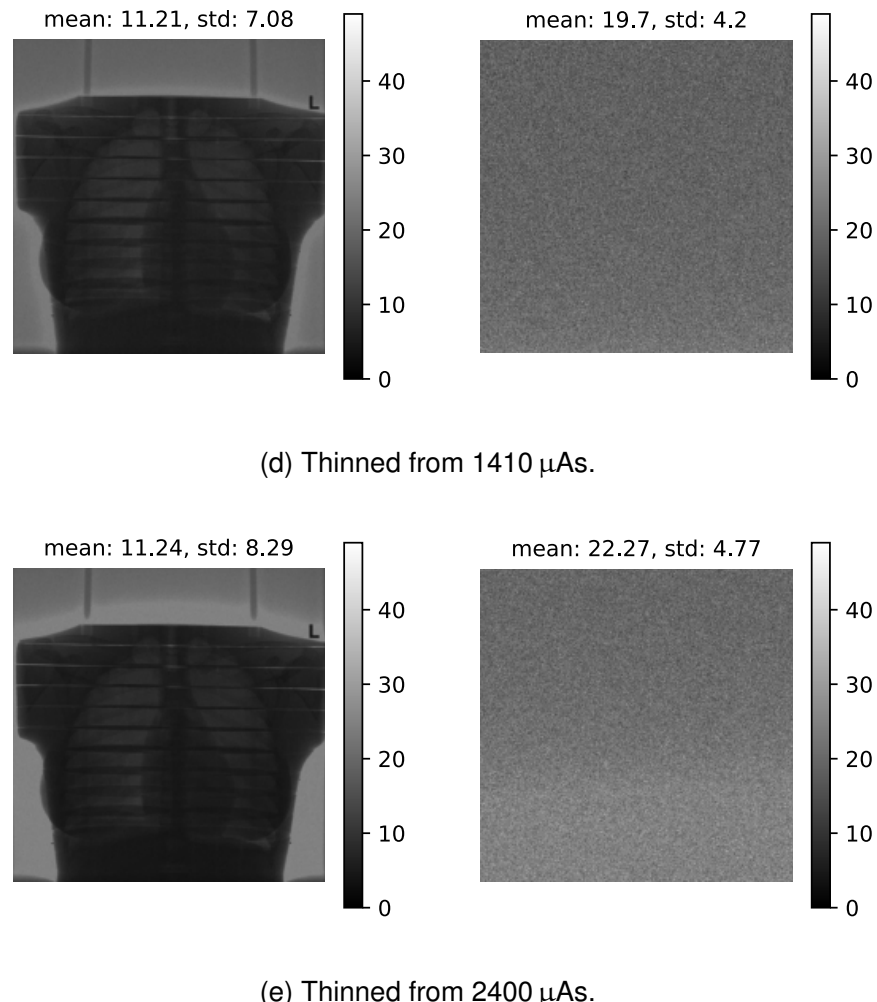
Figure 4.3: Phantoms thinned from different exposures to 600 µAs. For each original exposure ranging from 640 µAs to 2400 µAs the simulated low dose image is displayed together with a noise patch cut out of the image at the top between the two poles holding the phantom in place. Every image corresponds to a thinned version of Figure 4.2.
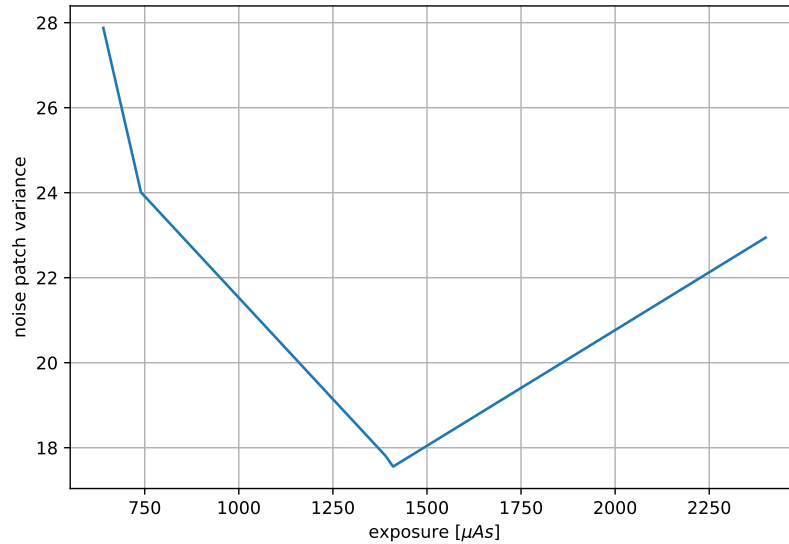
the simulated images and their noise patches are approximately identical between the simulations.

Quantitatively, the mean and variance of homogeneous noise patches are evaluated and plotted relative to each other in Figure 4.4 and Figure 4.5 for both phantom datasets. In both cases the variance converges towards the expected constant number, if simulated from higher exposures. For simulation from lower dose exposures, the variance of the simulated images is slightly higher than expected. In general, mean and variance witness only small variations. In an ideal case, mean and variance would be identical in all simulations, resulting in a point if variance and mean are plotted relative to each other. In reality, in Figure 4.4 the plot appears to be a short line, showing that despite imperfections, the simulation gives adequate results.
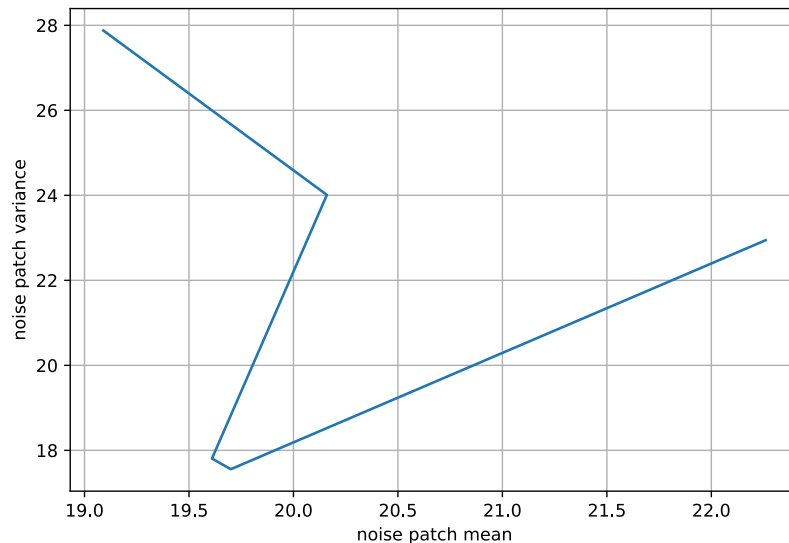
A similar attempt was made to simulate lower doses for the AirOnly dataset. The problem is that even for slightly higher doses, air does not provide enough attenuation anymore, so that the signal at the detector exceeds the detectable limits. This technical limitation manifests itself in clipped constant values, without any variance. It appears that the device is constructed and, therefore, probably adjusted for attenuation levels of human tissue and is not designed for air radiographs. This rendered the AirOnly data much less usable than initially expected and made their use for calibration similar to [2] impossible.

Figure 4.6 shows the results of thinning applied to a PNG image of the neural network training dataset. Even for extreme thinning to a simulated exposure of $0.1\,\mu As$ the result appears qualitatively close to the expected reality. Although most of the simulation is black, some clusters of white pixels can be recognized between if the image is displayed on a screen that provides enough contrast. These noisy clusters are only visible in areas where the original image showed a high exposure, namely the air background and the lungs.

In addition, an overview of the simulation results of the same image for different values of the simulation parameters for the simulated exposure (`sim_muas`) and the electronic noise variance (`eln_var`) is visualized in Figure 4.7. The images are qualitatively close to the expectation, while they are not evaluated quantitatively due to the coarse assumptions about the parameters.
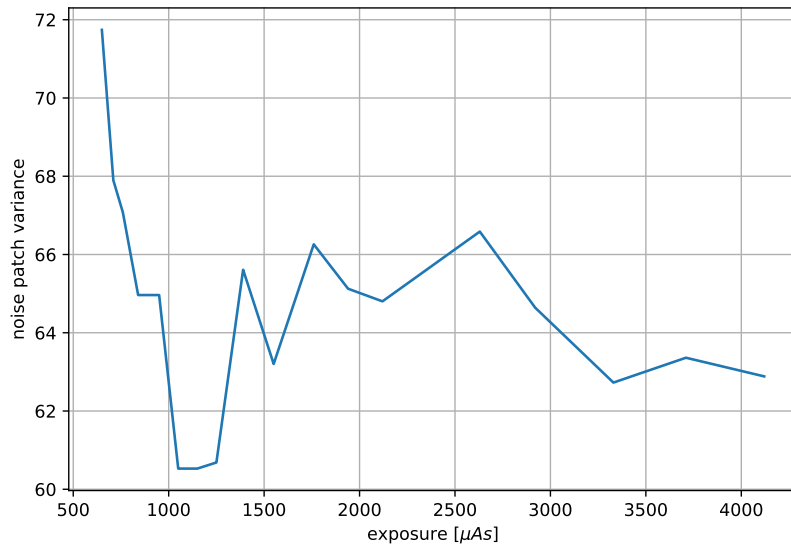
(a) Relation between original exposure before thinning and variance in thinned noise patches.
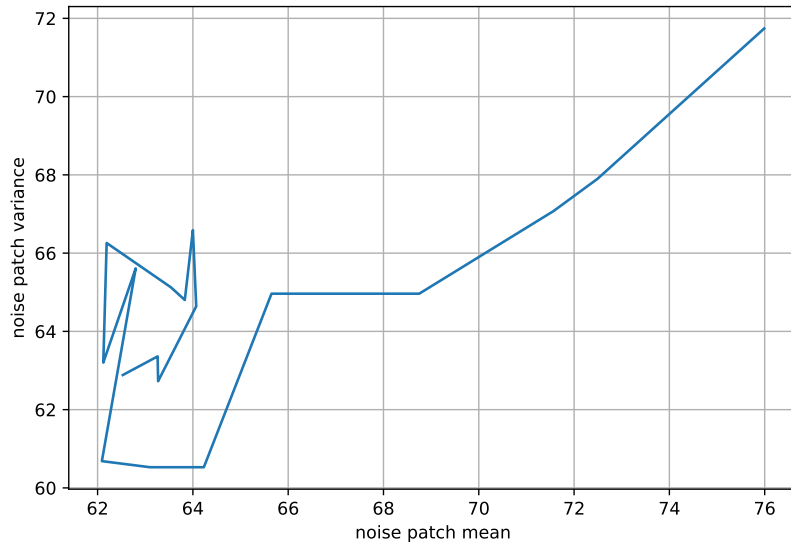

(b) Relation between mean and variance in noise patches. The data points are evaluated for every original exposure and connected in that order.

Figure 4.4: Quantitative results of photon thinning applied to new phantom radiographs. Visualized are the statistical parameters of the noise patches in Figure 4.3.
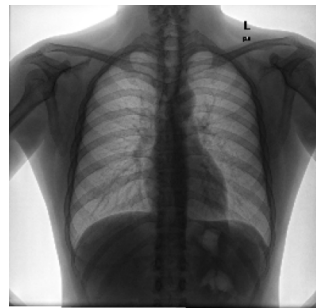
(a) Relation between original exposure before thinning and variance in thinned noise patches.
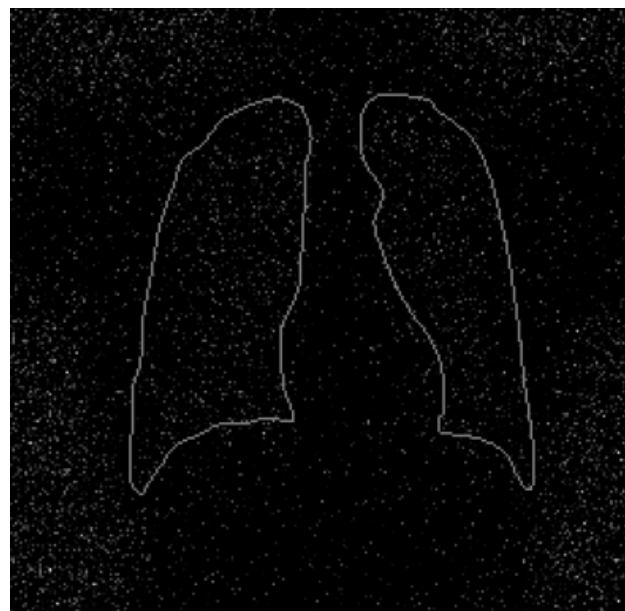
(b) Relation between mean and variance in noise patches. The data points are evaluated for every original exposure and connected in that order.

Figure 4.5: Quantitative results of photon thinning applied to PhantomNoAir dataset. The chosen noise patch for calibration and plotting is a homogeneous patch between the ribs with as few attenuation as possible.

(a) Sample image of the dataset for the neural network of unknown exposure.

(b) Sample image thinned to a simulated exposure of 0.1 µAs with an electronic noise variance of 10000. Additionally, the contour of the mask is added as a reference. The results should be understood only qualitatively because no quantitative calibration could have been performed.

Figure 4.6: Extreme thinning applied to a sample image of the neural network dataset. The original and thinned image are shown, where the thinned image requires a good contrast to be visible to humans.
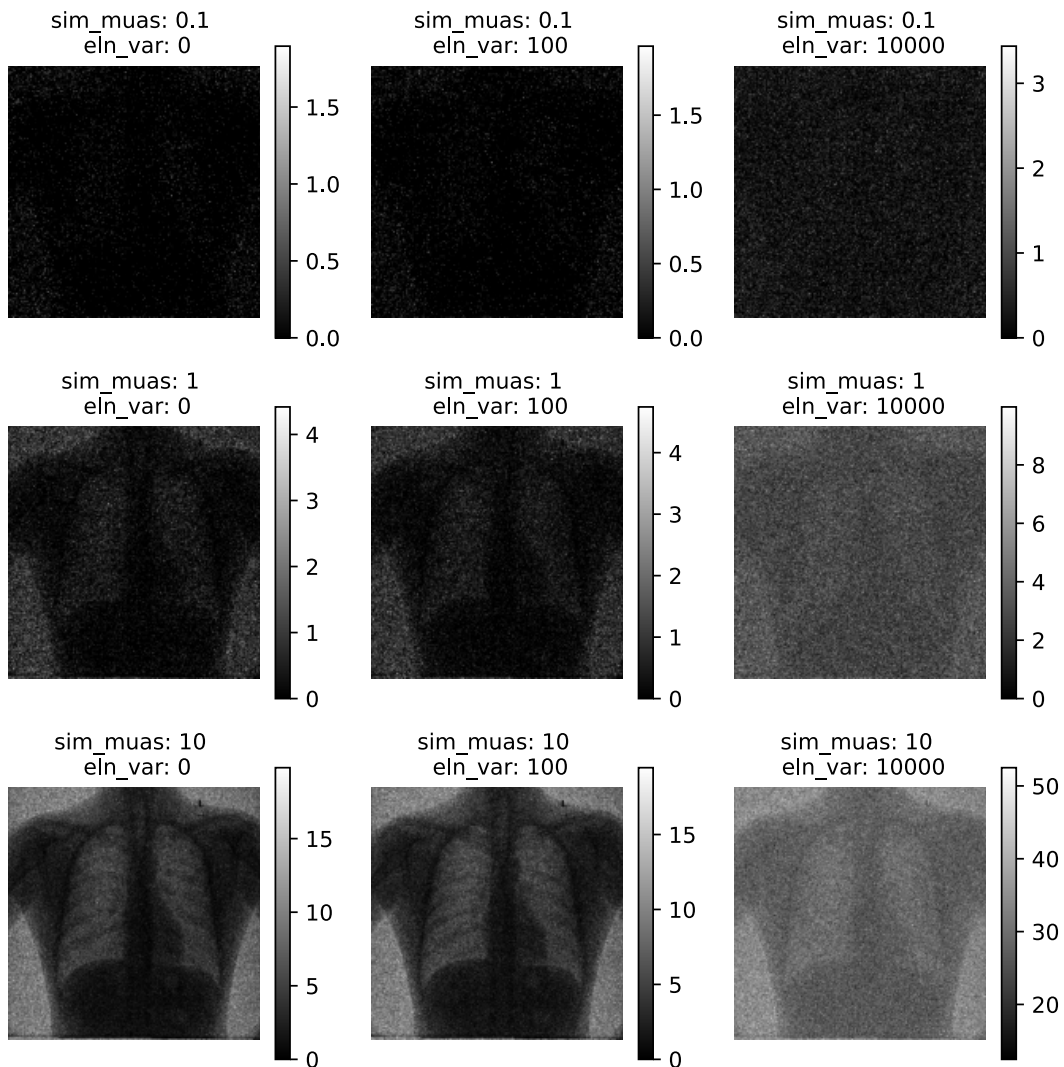
Figure 4.7: Overview of different low dose simulations applied to a sample image from the dataset of the neural network. The sample image is assumed to have a exposure of 4000 µAs. All different combinations of three different values for the simulated exposure (`sim_muas`) and the electronic noise variance (`eln_var`).
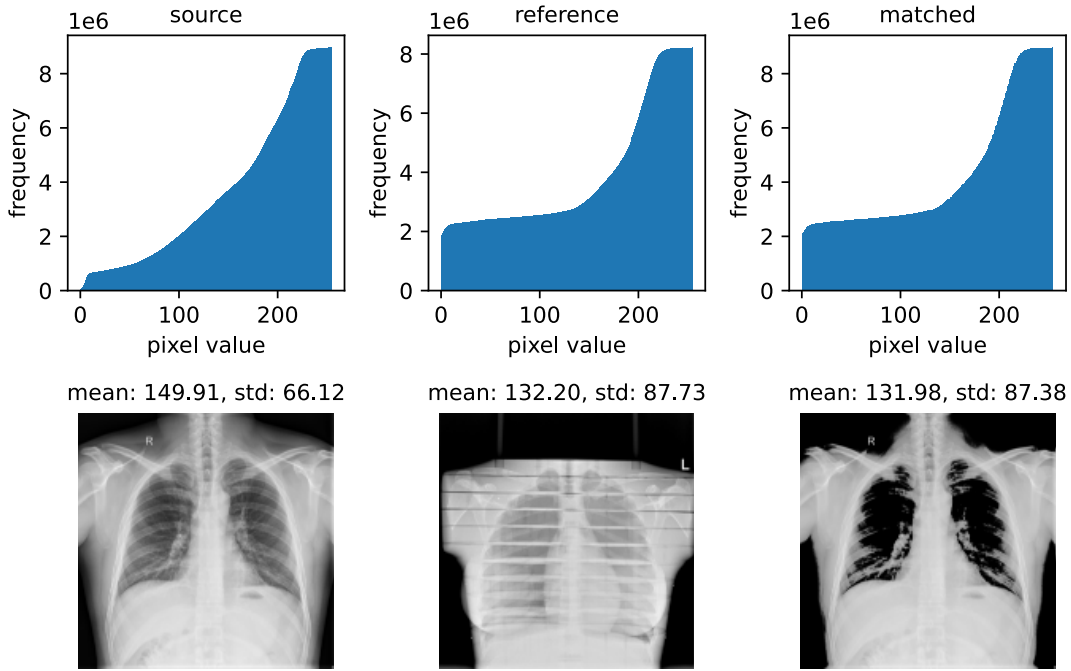
Figure 4.8: Result of histogram matching applied to an example image of the dataset using a PhantomAir image as reference. The source, reference and matched images are shown in combination with their histograms.

4.2 Comparison between Simulation and Baseline

The histogram matching as the given baseline approach for low-dose simulation was evaluated in [11] using the lowest dose radiograph of the old phantom data. Compared to most of the images in the training dataset, the PhantomNoAir data covered almost no surrounding air padding. Therefore, this section starts with an evaluation of histogram matching using the new phantom radiograph with an equivalent exposure as previously introduced in section 3.1. As shown in Figure 4.8, the baseline approach fails to achieve a proper simulation in this case, because the histogram matching is based only on visual image information. Even worse, the additional air padding in the reference causes the histogram matching to highlight the lung, because these pixels are mapped to the same black value as the air background by matching.

Even if the old phantom is used as a reference, the visual contrast of the image obtained by histogram matching is reduced relative to the original. However, most
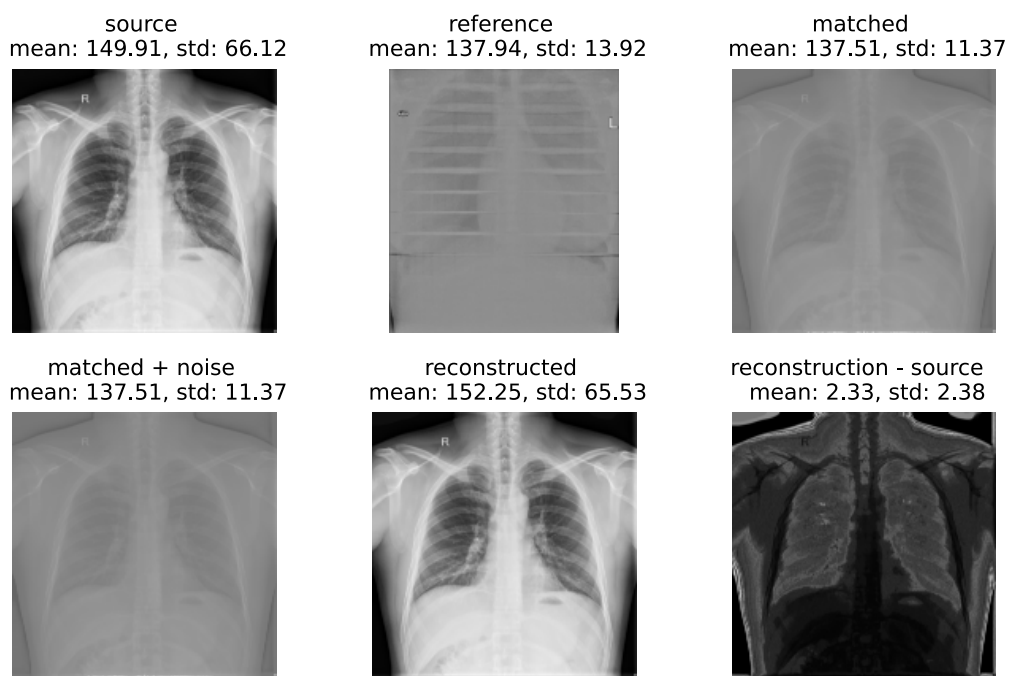
Figure 4.9: Reconstruction of a histogram matched image without noise by application of histogram matching using the source image as reference. The difference between reconstruction and original source is shown in the lower right image.
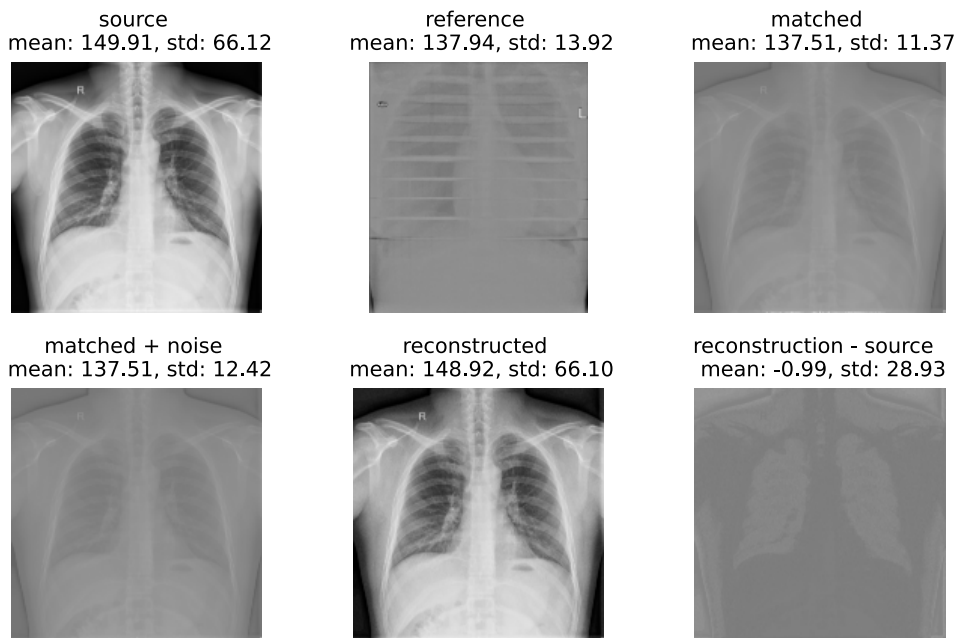
of the information survives histogram matching, which can then be reconstructed by application of another histogram matching given the original histogram or histogram equalization. Without additional noise, the reconstructed image is almost identical to the original as shown in Figure 4.9. The only differences occur when two pixel values are mapped to the same value by histogram matching, due to the limited possibilities of integer values. For all other pixel values, the matched image contains exactly the same structural information available to the neural network, but the reduced contrast makes identification by human eyes more difficult. Hence, it is not surprising that there is a direct correspondence between the added noise and the difference between the original and reconstructed images, as shown in Figure 4.10. The addition of gaussian noise only partially affects the image quality while application of Poisson noise results in a more notable modification. This loss in information manifests itself in the difference between the reconstructed image and the source image.

## 4.3 Evaluation of the Neural Network
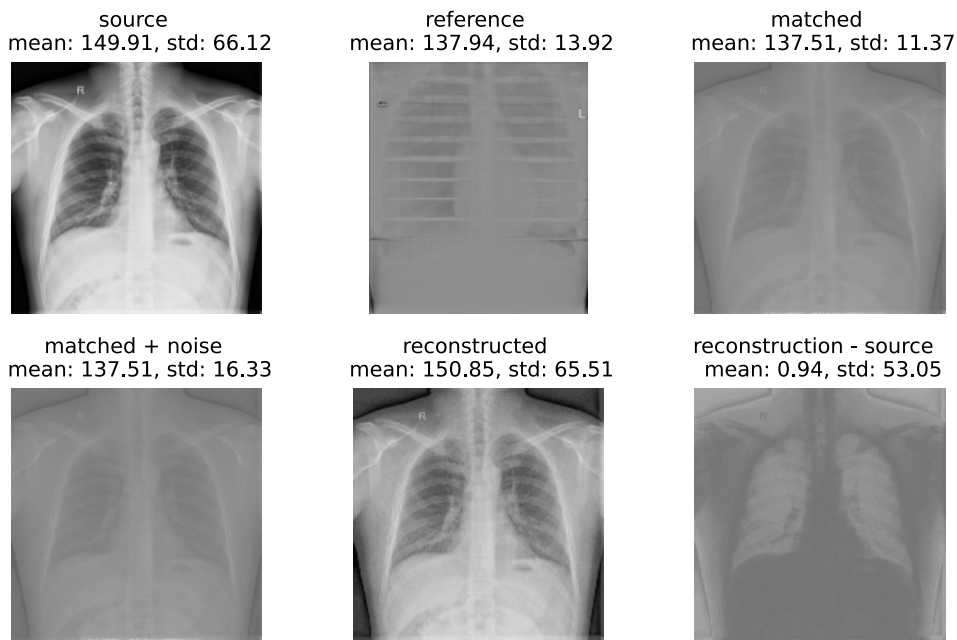
As described in section 3.3, a U-net was trained on thinned images at different parameters. The results in the form of different metrics evaluated with the test images are depicted in Figure 4.11. The performance of the network decreases for lower simulated doses, as well as for increased electronic noise. For a parameter configuration that results in medium values in the performance metric, two example segmentation outputs are compared to the original mask in Figure 4.12. As can be seen, a good FOV detection can even be achieved for a suboptimal segmentation.

The most interesting evaluation of the resulting overreach, underreach and FOV reduction is shown in Figure 4.13 and Figure 4.14. The higher quality simulation of a higher exposure and no noise in Figure 4.14 results in a good FOV detection if no tolerance is added, but only with an additional tolerance around the detected FOV critical underreach can be eliminated mostly. With tolerance, the higher quality simulation still results in a noticeable reduction in FOV.

The lower quality simulation of a lower dose and higher noise in Figure 4.13 peaks at a lower FOV reduction even without added tolerance. For this simulation if tolerance is added to avoid underreach, the FOV reduction gives poor results where

(a) Reconstruction of a histogram matched image after added gaussian noise.

(b) Reconstruction of a histogram matched image after applied Poisson noise.

Figure 4.10: Results of reconstruction attempts of histogram matched images with different kinds of added noise.

(a) Segmentation accuracy.

(b) BCEWithLogitsLoss.

(c) Dice score.

(d) Box Intersection over Union.
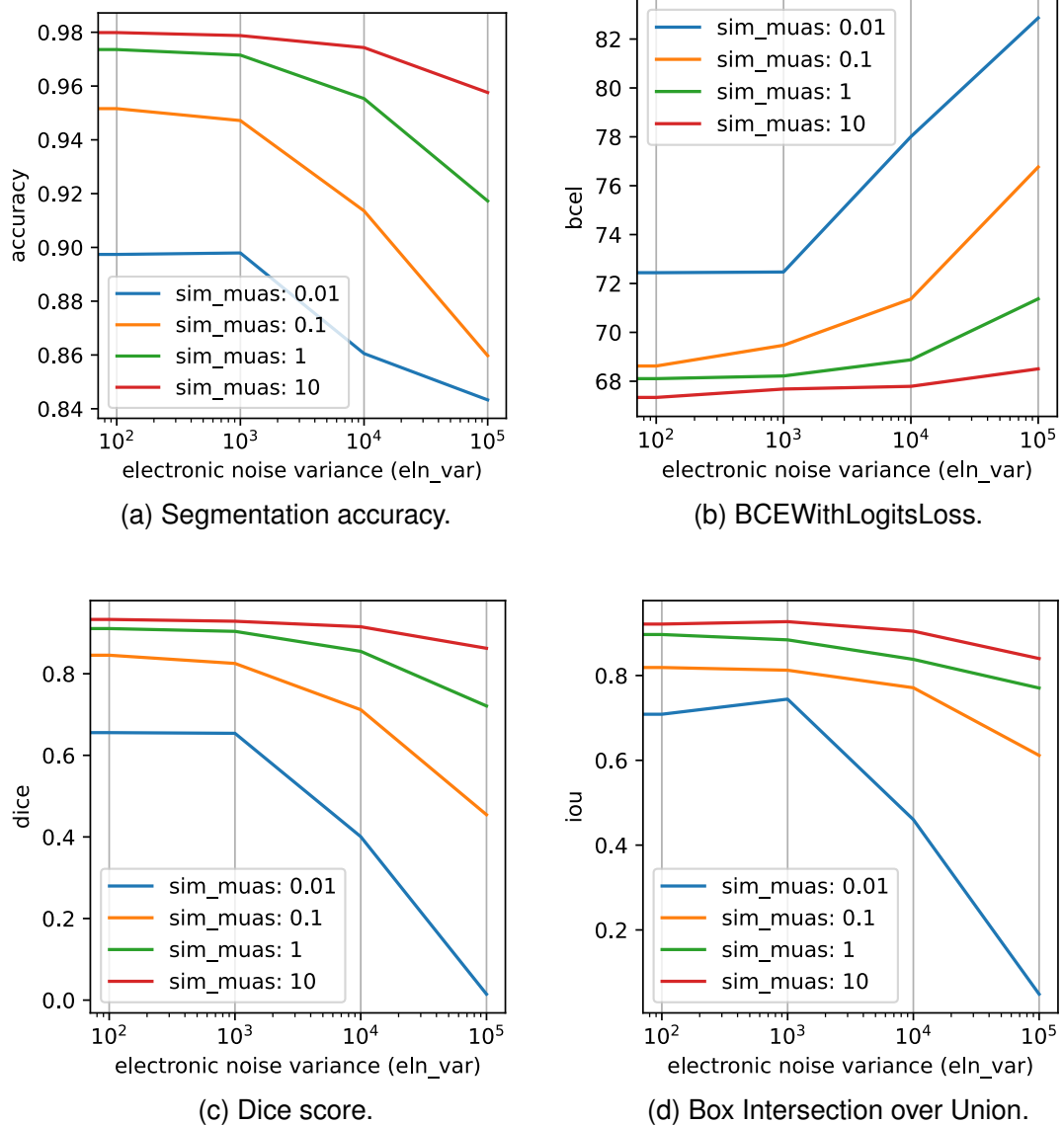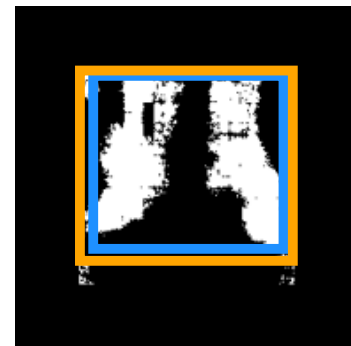
Figure 4.11: Different metrics of U-net performance on test dataset for different simulation parameters.
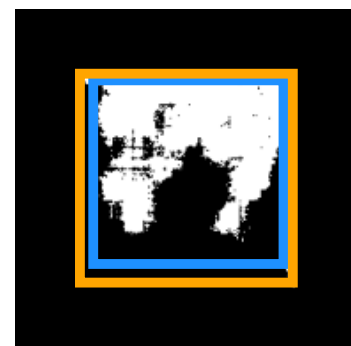
(a) Reference mask.

(b) Good segmentation | good bounding box.
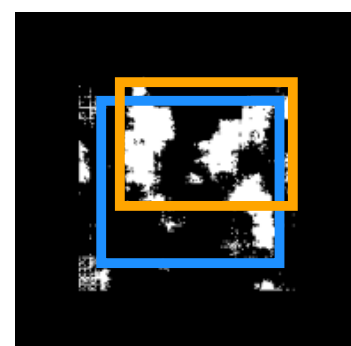
(c) Reference mask.

(d) Bad segmentation | good bounding box.

(e) Reference mask.

(f) Bad segmentation | bad bounding box.

Figure 4.12: Example U-net outputs with reference (blue) and predicted (orange) bounding box. Simulation at `sim_muas`=0.1, `eln_var`=10000.

even significantly many negative values are encountered, where the FOV should even be extended out of the current range by the added tolerance. Despite the low performance in FOV reduction, several occurrences of underreach remain even with tolerance.

(a) Overreach without tolerance.

(b) Underreach without tolerance.

(c) Overreach with tolerance.

(d) Underreach with tolerance.

(e) FOV reduction without tolerance.

(f) FOV reduction with tolerance.
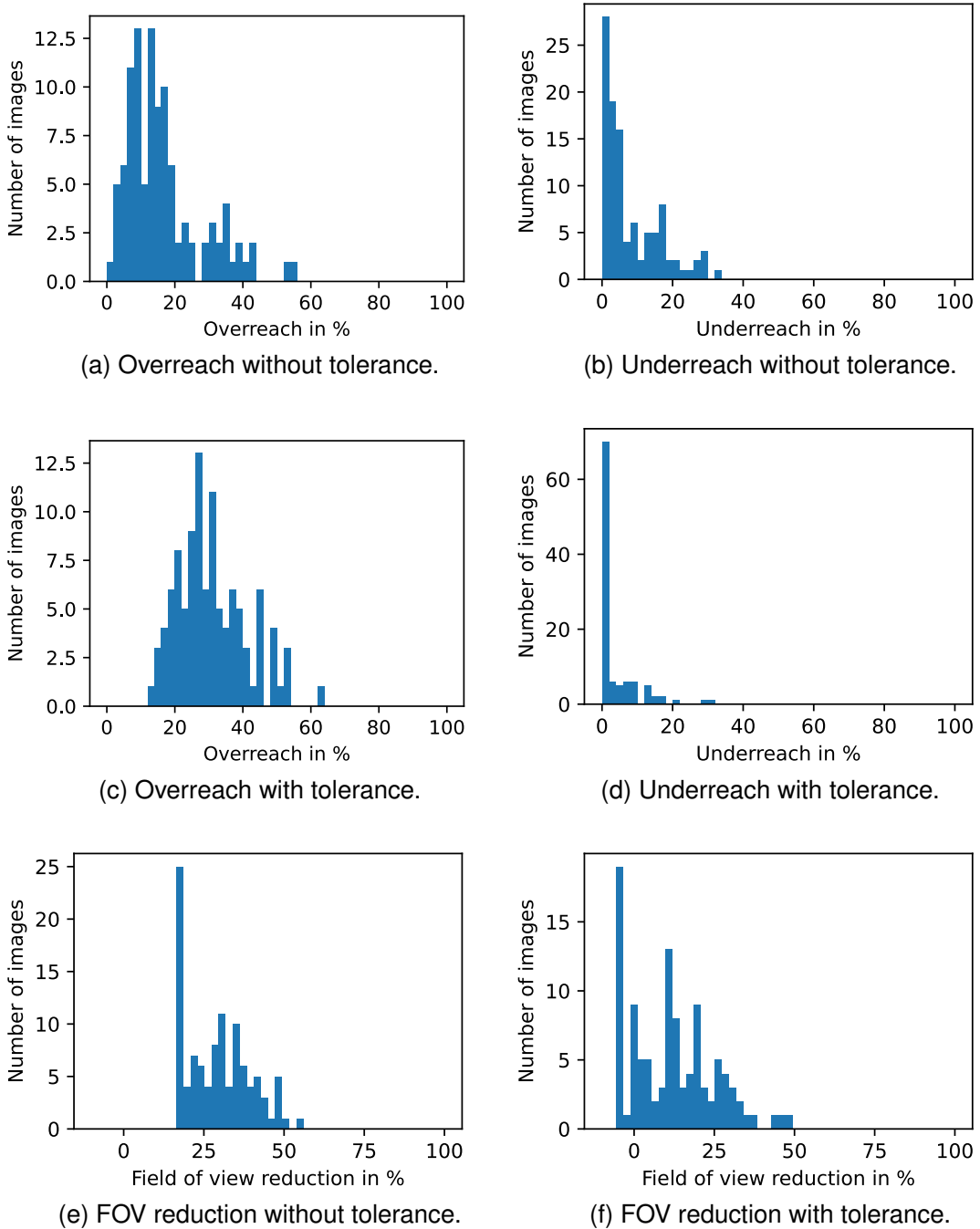
Figure 4.13: Evaluation of overreach, underreach and FOV reduction of the U-net with lower quality simulation at `sim_muas=0.1`, `eln_var=10000`.

(a) Overreach without tolerance.

(b) Underreach without tolerance.

(c) Overreach with tolerance.

(d) Underreach with tolerance.

(e) FOV reduction without tolerance.

(f) FOV reduction with tolerance.
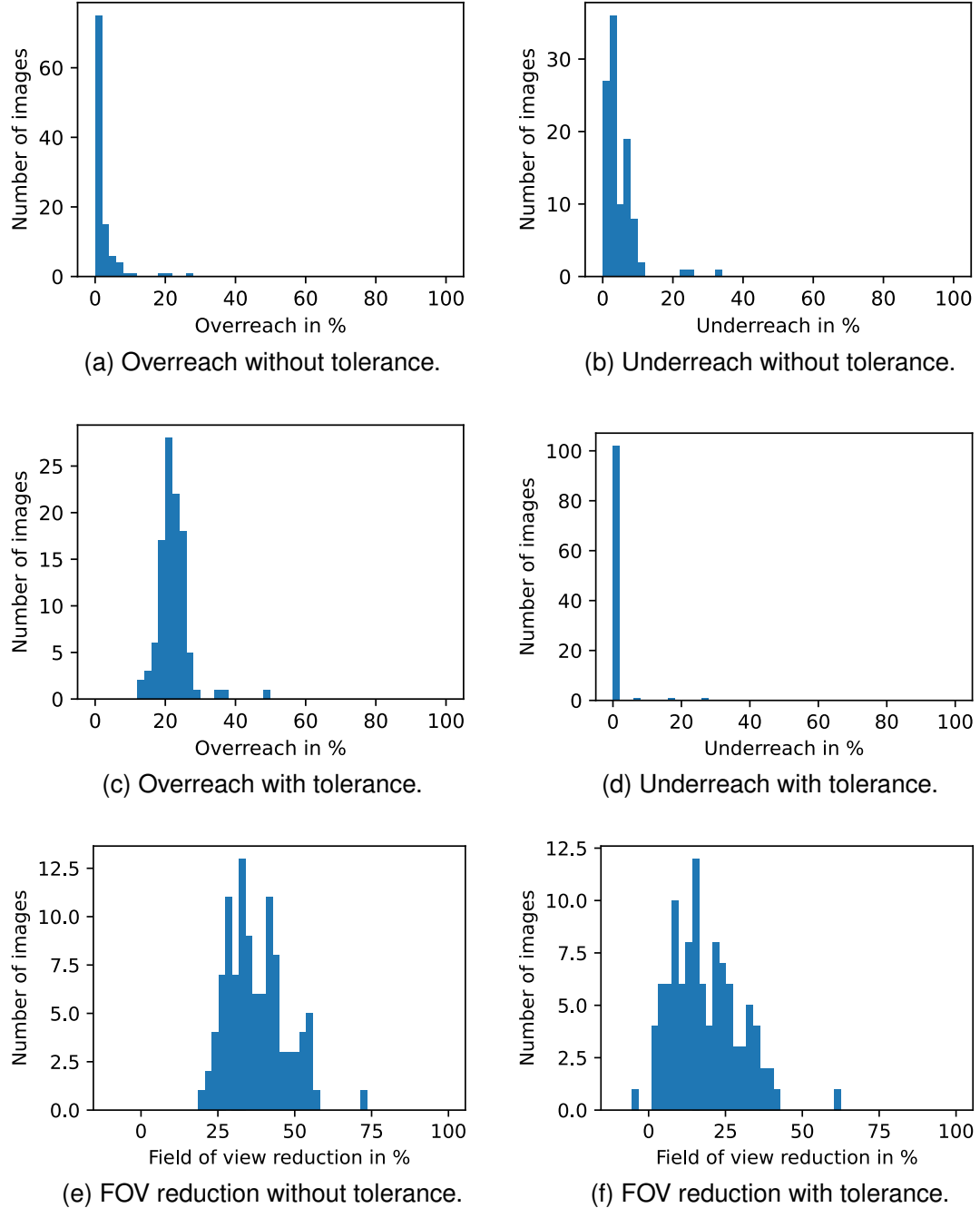
Figure 4.14: Evaluation of overreach, underreach and FOV reduction of the U-net with higher quality simulation at `sim_muas=10`, `eln_var=0`.

5 Discussion

The baseline approach simulates low-dose radiographs purely in the image domain. The histogram matching and the added noise can be directly applied to visual images in any common file format. Less calibration is necessary, as a single reference image of the desired dose and the parameters of additional noise need to be specified. This advantage of the baseline allows it to be applied to almost any image dataset, whether it contains image data only or additional information in DICOM files.

However, this simplicity in implementation and application comes at costs. The reduction of image contrast by histogram matching does not consider the underlying physical processes for x-rays, resembling a less realistic and physically inaccurate simulation. It can easily be distracted by air padded references, up to a degree where it is rendered unsuitable for simulation, as demonstrated in section 4.2. Moreover, the information contained in the simulated images is mostly only modified by the application of Poisson. Except for that noise, most of the information is easily reconstructible and therefore still available to the neural networks evaluated in [11].

The previous work [11] assumes a noise model, where Poisson noise can be applied directly to the images, where every pixel is mapped following a Poisson distribution, given a parameter λ equal to the value of the pixel. Given the physically inspired noise model of [2] used in this work, the Poisson parameter is the medium rate of photons. This photon rate is higher with more incident x-rays, resulting in a Poisson variance equal to λ that increases linearly with the intensity. In images resulting from radiography, the intensity is depicted in a inverse way. Therefore, the Poisson noise should be applied more realistically to the inverse of the image.

Another disadvantage of the baseline simulation is that the noise model is applied to the images as if there was no noise before. In reality, the higher dose images follow the noise model already. Instead of adding a simulated quantum and elec-

tronic noise to the image, the binomial distribution photon thinning in [2] takes into account that both kinds of noise are already present in the original. The application of the binomial distribution already reduces the quantum noise accordingly, and the only noise added is there to compensate for the constant electronic noise, which is accidentally reduced by the binomial distribution as well.

In summary, this lack of physical plausibility in low-dose simulation might be a reason why the neural networks evaluated in [11] showed unexpectedly good performance even for extremely noisy images.

The new simulation approach of photon thinning, adapted and implemented in this thesis, is more realistic because it inherently considers the underlying physical models. Furthermore, it takes into account that the original radiographs already contain noise.

A disadvantage of the new simulation is the more complex calibration individually for every x-ray device. When internal details about the device are unknown and not provided by the manufacturer, attempts must be made to reverse engineer parts of the post-processing like in section 3.2 to work with data that are as raw as possible. Especially information about the noise calibration, which is relevant for calibration, is commonly reduced by post-processing.

In addition to the device specific calibration, radiography meta information such as the exposure applied during recording must be knwon to simulate a specific exposure because the binomial distribution must be parametrized accordingly. This parameter of the measurement process is difficult to estimate from pure images, for which reason DICOM data is required for a quantitatively accurate simulation.

Attempts to estimate calibration parameters automatically by special radiographs attenuated only by air or without the presence of x-rays did not give the expected results. Quantum noise could not be estimated by air measurements, because the values already converged to a limit for relatively low exposures. Electronic noise could not be estimated using no x-ray measurements, because the device interface did not provide an option for that. And, as seen in Figure 3.1, even when the x-ray tube is covered by one or two lead aprons, structural information is still visible on the detector, suggesting that there are still a significant amount of x-rays left. Therefore, calibration had to be performed using homogeneously attenuated patches on radiographs of different exposures, as explained in section 3.2.

The new simulation has two advantages, which justify the additional effort. On the one hand, its physical plausibility. On the other hand, two images can be fused easily by simply adding their photon representation. The latter is especially useful for the long term goal of reducing x-ray doses by FOV detection. A low dose image can be taken, the FOV is analyzed by a neural network, and a second image is taken at a higher dose restricted to the desired region of interest. If two images of different doses can be fused, the whole x-ray exposure is used effectively and full quality is offered to clinicians for diagnosis. This is more difficult to achieve in the image domain, where it does not correspond to a plain addition.

In summary, the new simulation gives physically more realistic results and is therefore better suited to produce meaningful results. However, it is difficult to apply the new approach to analyze the performance of a neural network due to the increased requirements listed in the following paragraph. These requirements are prerequisites that must be met for training data such that their low-dose equivalent can be quantitatively simulated. Especially the fact that the device and its calibration parameter as well as the measurement exposure for every image would need to be known, makes it impractical to be used with image only datasets, like the one with segmentation labels that is publicly available and used in [11].

For a realistic quantitative evaluation, a dataset must be found or collected that is large enough, contains enough meta data such as DICOM files, contains radiographs performed by a known device with respective calibration parameters, and provides labels such as the corresponding segmentation that are required to train the neural networks. The fact that such a dataset was not found for lung segmentation limited the opportunities to analyze the impact of the new simulation on the performance of the neural networks.

However, making some assumptions about the radiographs stored as PNG images in the available segmentation dataset used made at least an approximate qualitative evaluation of thinning on these x-rays possible. The results of this thinning are consistent with the expected behavior, indicating that it can be used for a meaningful first qualitative evaluation of the performance of neural networks on low dose images using the new simulation approach. Until now only the best performing MONAI U-net from [11] has been used with the new simulation and only a segmentation has been trained. The reason for this selection are the results in [11] that the MONAI U-net gives good results at a moderate number of parameters and that

segmentation performs better than keypoint detection.

The performance of the U-net has explicitly been evaluated for simulations of two different qualities. For higher quality simulation at higher exposure with no noise, the U-net performed well and resulted in a useful reduction in FOV. For the lower quality simulation at lower exposure and higher noise, the U-net gave insufficient results in FOV reduction, while still being affected by underreach even with tolerance.

The test metrics on the U-net, such as segmentation accuracy, were different but promising for both sets of simulation parameters. Still, they performed significantly differently in terms of FOV detection and therefore its reduction as well. On the other hand, even for bad segmentation results, FOV detection often succeeds better than expected for the segmentation. This motivates the possibility that the correlation between segmentation and FOV might not be as high as originally assumed.

The effort that has been put into the creation of a flexible and extensible python package with less code redundancy should be understood as a preparation for further experiments in the future and is an investment to facilitate possible future work in this area. In particular, the features of the package explained in section 3.4 offer various advantages over the previous code base.

The use of hashes to identify neural networks and parameters increases traceability and distinguishability between different network configurations that are trained and evaluated. The need to assign speaking names to files manually is replaced by a self-explaining hash value that can be used to look up all relevant parameters. Moreover, it allows "training on demand" in evaluation scripts, by looking up if training has already been performed for the hash of a given architecture configuration. If this is the case, the values can be loaded automatically or the training can be directly started, otherwise, before the evaluation takes place. The possibility of running evaluations for single hashes without additional description results in transparent evaluation code fully independent of architecture details, which are automatically loaded.

Separation of data and operations in `OperableData` allows it to be easily extended. It can be used flexibly and transparently for different types of underlying data by assigning different operations. This means that for example, in the code for this thesis DICOM and PNG files can handled mostly interchangeably by `OperableData` with different implementations for the same operations.

6 Conclusion

A physically realistic simulation is an essential foundation for meaningful results. This is especially the case, because the performance evaluation of the neural networks of [11] depends on the quality of the simulation. The histogram matching as the baseline approach in [11] lacks plausibility, as demonstrated in section 4.2. The physically inspired approach to simulate low-dose CT scans in [2] was adapted to conventional x-rays in section 3.2 and showed promising results in section 4.1. The advantages and disadvantages as discussed in chapter 5 show that the new simulation approach is better suited to simulate low dose radiographs from normal dose x-rays. However, photon thinning requires more effort in calibration and puts other requirements on training data, which inspires additional possibilities for future work. The first evaluation of neural network performance on photon thinned images in section 4.3 shows promising results for a qualitatively realistic simulation depending on the simulation parameters.

6.1 Future Work

Additional possible improvements described in [2] such as compensation for noise correlation or beam hardening effect should be further investigated to determine whether they should also be incorporated into the simulation.

In addition, more variations in the neural network can be evaluated to improve them and their impact on the reduction of the x-ray dose. This could not be done in this work as planned at the beginning, because the more complex simulation and the proper implementation was more time consuming than initially expected.

Another possibility to further evaluate the new simulation is to extend the Python package using the keypoint detection models of [11]. The implementation is already

prepared, so that extensions can be implemented more intuitively. The advantage of keypoint detection is that it uses a dataset provided locally by the Ulm University Hospital. Therefore, the device can be determined, calibrated if different from the device in this work, and the data is generally available as DICOM files. This work focused on segmentation, as it promised better results based on [11], but maybe the keypoint detection can give more insight.

Ideally, the labels of the local DICOM dataset would be extended by segmentation in addition to the already available keypoints, as postulated by [11]. This would also allow the new simulation to be evaluated with segmentation, and even result in a more fair comparison between segmentation and keypoint detection.

As [11] already mentions, the concept might be applied not only to lung detection on thorax x-rays but also to other dedicated areas such as other organs or joints. The results of this thesis showed that extending the reference by some padding before the histogram matching resulted almost directly in a quite good segmentation using only traditional computer vision. This motivates the assumption that the contrast between the lung and other tissues in a human thorax is relatively high. An analysis of whether this performance can be achieved with other organs in a similar manner could better differentiate between the impact of the application of neural networks and the difficulty of the task.

The observation that segmentation and FOV might not correlate as much as initially assumed motivates more data science and statistics that should be performed in any further research. A better understanding of the relationship between them might improve ideas for further approaches.

Taking into account that the simulation used in this thesis is based on a low dose simulation of CT scans, the same idea of FOV reduction could be extended to CT as well. The foundation for the simulation is already available in [2]. Although the extension to CT data makes it more complex, the potential for more insight and a higher radiation reduction potential appear promising.

Finally, a collaboration with a manufacturer of x-ray devices would further the possibilities. The internal knowledge of the device and its postprocessing would allow for a even better simulation. However, also since x-ray images are accumulated over a short time period, the ability to readout detector data at intermediate times should in theory provide real low-dose data during the recording of normal dose x-rays.

List of Figures

Bibliography

[1]   BfS. *Röntgendiagnostik: Häufigkeit und Strahlenexposition für die deutsche Bevölkerung*. Bundesamt für Strahlenschutz. Oct. 18, 2024. URL: `https://www.bfs.de/DE/themen/ion/anwendung-medizin/diagnostik/roentgen/haeufigkeit-exposition.html` (visited on 11/26/2025).

[2]   Masoud Elhamiasl and Johan Nuyts. "Low-dose x-ray CT simulation from an available higher-dose scan". In: *Physics in Medicine & Biology* 65.13 (July 2020). Publisher: IOP Publishing, p. 135010. ISSN: 0031-9155. DOI: `10.1088/1361-6560/ab8953`. URL: `https://doi.org/10.1088/1361-6560/ab8953` (visited on 11/26/2025).

[3]   Otto Glasser. *Wilhelm Conrad Röntgen und die Geschichte der Röntgenstrahlen*. Springer-Verlag, 2013.

[4]   Maximilian Glumann. *maximilian-glumann/master-thesis*. Nov. 26, 2025. URL: `https://github.com/maximilian-glumann/master-thesis` (visited on 11/26/2025).

[5]   Adam Jacobi et al. "Portable chest X-ray in coronavirus disease-19 (COVID-19): A pictorial review". In: *Clinical Imaging* 64 (Aug. 1, 2020), pp. 35–42. ISSN: 0899-7071. DOI: `10.1016/j.clinimag.2020.04.001`. URL: `https://www.sciencedirect.com/science/article/pii/S0899707120301017` (visited on 11/26/2025).

[6]   Stefan Jaeger et al. "Two public chest X-ray datasets for computer-aided screening of pulmonary diseases". In: *Quantitative Imaging in Medicine and Surgery* 4.6 (Dec. 2014), pp. 475–477. ISSN: 2223-4292. DOI: `10.3978/j.issn.2223-4292.2014.11.20`. URL: `https://pmc.ncbi.nlm.nih.gov/articles/PMC4256233/` (visited on 11/26/2025).

[7]   Thomas Kluyver et al. "Jupyter Notebooks – a publishing format for repro-
        ducible computational workflows". In: 20th International Conference on Elec-
        tronic Publishing (01/01/16). Ed. by Fernando Loizides and Birgit Scmidt. In
        collab. with Thomas Kluyver et al. IOS Press, 2016, pp. 87–90. DOI: `10.3233/`
        `978-1-61499-649-1-87`. URL: `https://eprints.soton.ac.uk/403913/`
        (visited on 11/26/2025).

[8]   M. Kreuzer. "Krebsrisiko durch ionisierende Strahlung im Niedrigdosisbere-
        ich". In: *Der Radiologe* 57.7 (July 1, 2017), pp. 517–518. ISSN: 1432-2102.
        DOI: `10.1007/s00117-017-0220-4`. URL: `https://doi.org/10.1007/`
        `s00117-017-0220-4` (visited on 11/26/2025).

[9]   *Lung Masks for Shenzhen Hospital Chest X-ray Set*. URL: `https://www.kag`
        `gle.com/datasets/yoctoman/shcxr-lung-mask` (visited on 11/26/2025).

[10]   E. A. Nekolla et al. "Häufigkeit und Dosis diagnostischer und interventioneller
        Röntgenanwendungen". In: *Der Radiologe* 57.7 (July 1, 2017), pp. 555–562.
        ISSN: 1432-2102. DOI: `10.1007/s00117-017-0242-y`. URL: `https://doi.`
        `org/10.1007/s00117-017-0242-y` (visited on 11/26/2025).

[11]   Alexander Ortlieb. "Optimal Field-Of-View in Low-Dose X-Ray Lung Imaging".
        MA thesis. Universität Ulm, Nov. 1, 2024.

[12]   Alexander Ortlieb. *Turadon/Master-thesis*. Nov. 1, 2024. URL: `https://gith`
        `ub.com/Turadon/Master-thesis` (visited on 11/26/2025).

[13]   Sivaramakrishnan Rajaraman et al. "Improved Semantic Segmentation of Tu-
        berculosis—Consistent Findings in Chest X-rays Using Augmented Training
        of Modality-Specific U-Net Models with Weak Localizations". In: *Diagnos-
        tics* 11.4 (Mar. 30, 2021). ISSN: 2075-4418. DOI: `10.3390/diagnostics`
        `11040616`. URL: `https://www.mdpi.com/2075-4418/11/4/616` (visited
        on 11/26/2025).

[14]   David B. Richardson et al. "Risk of cancer from occupational exposure to
        ionising radiation: retrospective cohort study of workers in France, the United
        Kingdom, and the United States (INWORKS)". In: (Oct. 20, 2015). DOI: `10.`
        `1136/bmj.h5359`. URL: `https://www.bmj.com/content/351/bmj.h5359.`
        `abstract` (visited on 11/26/2025).

[15] J. Anthony Seibert. "X-Ray Imaging Physics for Nuclear Medicine Technologists. Part 1: Basic Principles of X-Ray Production". In: *Journal of Nuclear Medicine Technology* 32.3 (Sept. 1, 2004), pp. 139–147. ISSN: 0091-4916, 1535-5675. URL: `https://tech.snmjournals.org/content/32/3/139` (visited on 11/26/2025).

[16] J. Anthony Seibert and John M. Boone. "X-Ray Imaging Physics for Nuclear Medicine Technologists. Part 2: X-Ray Interactions and Image Formation". In: *Journal of Nuclear Medicine Technology* 33.1 (Mar. 1, 2005), pp. 3–18. ISSN: 0091-4916, 1535-5675. URL: `https://tech.snmjournals.org/content/33/1/3` (visited on 11/26/2025).

[17] Sergii Stirenko et al. "Chest X-Ray Analysis of Tuberculosis by Deep Learning with Segmentation and Augmentation". In: *2018 IEEE 38th International Conference on Electronics and Nanotechnology (ELNANO)*. 2018 IEEE 38th International Conference on Electronics and Nanotechnology (ELNANO). Apr. 2018, pp. 422–428. DOI: `10.1109/ELNANO.2018.8477564`. URL: `https://ieeexplore.ieee.org/abstract/document/8477564` (visited on 11/26/2025).

[18] *Trixell Detector Technical Specifications*. URL: `https://www.trixell.com/sites/default/files/upload/files/txl_pixium_4343.pdf` (visited on 11/26/2025).